

A SURVEY OF H₂O, CO₂ AND CO ICE FEATURES TOWARDS BACKGROUND STARS AND LOW MASS YSOS USING AKARI.¹

J. A. NOBLE²

Aix-Marseille Université, PIIM UMR 7345, 13397, Marseille, France.

H. J. FRASER²

Department of Physical Sciences, The Open University, Walton Hall, Milton Keynes MK7 6AA, United Kingdom.

Y. AIKAWA

Department of Earth and Planetary Sciences, Kobe University, Kobe 657-8501, Japan.

K. M. PONTOPPIDAN

Space Telescope Science Institute, 3700 San Martin Drive, Baltimore, MD 21218, U.S.A.

AND

I. SAKON

Department of Astronomy, Graduate School of Science, University of Tokyo, 7-3-1 Hongo, Bunkyo-ku, Tokyo 113-0003, Japan.

Draft version September 23, 2018

ABSTRACT

We present near infrared spectroscopic observations of 19 molecular clouds made using the AKARI satellite, and the data reduction pipeline written to analyse those observations. The 2.5 – 5 μm spectra of 30 objects – 22 field stars behind quiescent molecular clouds and eight low mass YSOs in cores – were successfully extracted using the pipeline. Those spectra are further analysed to calculate the column densities of key solid phase molecular species, including H₂O, CO₂, CO, and OCN⁻. The profile of the H₂O ice band is seen to vary across the objects observed and we suggest that the extended red wing may be an evolutionary indicator of both dust and ice mantle properties. The observation of 22 spectra with fluxes as low as < 5 mJy towards background stars, including 15 where the column densities of H₂O, CO and CO₂ were calculated, provides valuable data that could help to benchmark the initial conditions in star-forming regions prior to the onset of star formation.

Subject headings: astrochemistry — infrared:stars — ISM:clouds — ISM:abundances — ISM:molecules — stars:formation

1. INTRODUCTION

The three most abundant solid phase molecular species in the interstellar medium (ISM) are H₂O, CO₂, and CO. The strongest absorptions of all three species are seen in the 2.5 – 5 μm region of the spectrum, associated with the stretching mode vibrations of each molecule. AKARI was the first space telescope since ISO with which it was possible to make spectroscopic observations of the full near infrared (NIR) range. Compared with *Spitzer* or ground-based observations, AKARI spectroscopy offers two distinct advantages: simultaneous observation of the stretching mode absorption bands of H₂O, CO₂, and CO, and observation of the blue wing of the H₂O stretching mode absorption. Two further benefits of AKARI are slitless spectroscopy, with spectra simultaneously captured for all objects in the field of view, and exceptional sensitivity, allowing observation of ice spectra on lines of sight towards objects with fluxes approaching 1 mJy.

We present a study of the 2.5 – 5 μm ice

absorption spectra towards background stars and young stellar objects (YSOs) with AKARI. To date, very few spectroscopic ice studies with AKARI have been published (see e.g. Shimonishi et al. 2008, 2010; Burgdorf et al. 2010; Yamagishi et al. 2011; Aikawa et al. 2012; Sorahana & Yamamura 2012) reflecting the difficulty of reducing AKARI spectral data. In all previous observations, ice spectra were derived from a single, relatively bright, object in the field of view. To study background star ice spectra, we have extracted data from multiple faint objects in a single observation, requiring the development of a unique data reduction pipeline.

The ultimate aim of our AKARI observing programme is to map the spatial distribution of the key ice species H₂O, CO₂, and CO. A prerequisite, however, is a robust data reduction and analysis method, to ensure the reliable determination of molecular ice column densities over hundreds of objects concurrently. The first aim of this article is to detail this analysis process. These data enhance the sample of ice spectra towards background stars and low mass YSOs; our second aim is to test how the chemical processes governing ice formation and evolution are related.

The chemistry of CO, CO₂, and H₂O in molec-

helen.fraser@open.ac.uk

¹Based on observations with AKARI, a JAXA project with the participation of ESA.

²Previous address: Department of Physics, Scottish Universities Physics Alliance, University of Strathclyde, Glasgow, G4 0NG, Scotland.

ular clouds is intrinsically linked. Solid H₂O is the dominant interstellar ice species, seemingly ubiquitous in the dense, molecular ISM (Leger et al. 1979; Whittet et al. 1983; Boogert et al. 2011). This H₂O forms on the surface of silicate dust grains (Tielens & Hagen 1982; Boogert & Ehrenfreund 2004; Miyauchi et al. 2008; Ioppolo et al. 2008; Dulieu et al. 2010), most likely through a combination of reactions involving H atoms, O atoms, and OH radicals.

Gas phase CO is highly abundant in molecular clouds and is commonly used to trace astrophysical conditions (e.g. van Kempen et al. 2009). However, unlike H₂O, CO accretes onto icy grain surfaces at a rate proportional to the gas density (e.g. Aikawa et al. 2001; Pontoppidan et al. 2003a), resulting in a CO-rich ice layer. Subsequently, as a function of time, temperature, or other energetic inputs to the ice mantle, the H₂O and CO layers can mix, producing a second CO ice environment, as illustrated by previous experimental (Collings et al. 2003a) and observational (Pontoppidan et al. 2003a) work. Both of these CO ice environments have been detected in interstellar observations (Tielens et al. 1991; Whittet & Duley 1991; Chiar et al. 1995; Pontoppidan et al. 2003a).

CO₂ is believed to form in the solid phase, based upon its low gas phase abundances (van Dishoeck et al. 1996). CO₂ ice has been observed towards numerous interstellar environments, including low mass YSOs (Nummelin et al. 2001; Pontoppidan et al. 2008) and background stars (Knez et al. 2005). Laboratory experiments prove that CO₂ formation is effective via several energetic (Gerakines et al. 1996; Palumbo et al. 1998; Jamieson et al. 2006; Mennella et al. 2004) and purely thermal (Goumans et al. 2008; Oba et al. 2010; Ioppolo et al. 2011; Noble et al. 2011; Zins et al. 2011) mechanisms. Recent results imply that the reaction CO + OH occurs in competition with H₂O formation (via H + OH), and that some CO molecules freeze-out from the gas phase long before CO ice is formed. Such postulations can only be tested through concurrent observations of CO, CO₂, and H₂O ices.

Any sample of ice spectra observed to date has been, necessarily, dictated by both the spectral range and sensitivity of IR telescopes. Low mass YSOs have therefore been rather more extensively studied than background stars, beginning with limited ISO observations (Guertler et al. 1996; de Graauw et al. 1996; Gerakines et al. 1999; Alexander et al. 2003). *Spitzer*, more sensitive than ISO, observed many more low mass YSOs (e.g. Gibb et al. 2004; Zasowski et al. 2009; Boogert et al. 2008). The *Spitzer* Legacy program ‘‘From Molecular Cores to Planet-Forming Disks’’ (c2d) extensively detailed the abundances of CO₂ (Pontoppidan et al. 2008), H₂O (Boogert et al. 2008), CH₄ (Öberg et al. 2008), and NH₃ (Bottinelli et al. 2010) ices towards a sample of 41 low mass YSOs, providing the largest dataset of column density values for these key interstellar molecules (Öberg et al. 2011). An important conclusion of this survey is that the abundances of the major ice species are remarkably similar in different star forming regions, although, for reasons not yet fully determined, the ice composition of minor and volatile species varies extensively. This suggests that ices

TABLE 1
MOLECULAR CORES OBSERVED

Core	Coordinates	Observation	Date
	R. A., Dec. /deg ^a	ID ^b	dd/mm/yy
L 1551	67.8708, +18.1356	3010019_001	28/02/07
B 35A	86.126, +9.1461	4120022_001 [†]	16/03/07
DC 269.4+03.0	140.5938, -45.7896	4120043_001	09/12/06
		4121043_001	08/06/07
DC 274.2-00.4	142.2042, -51.6153	4120007_001 [†]	17/12/06
DC 275.9+01.9	146.6904, -51.1000	4120009_001 [†]	20/12/06
DC 291.0-03.5	164.9663, -63.7227	4120023_001 [†]	21/01/07
BHR 59	166.7875, -62.0994	4120002_001 [†]	19/01/07
DC 300.2-03.5	186.0904, -66.2024	4121045_001 [†]	07/08/07
Mu 8	187.7146, -71.0227	4120018_001 [†]	12/02/07
DC 300.7-01.0	187.8771, -63.7233	4120024_001	02/02/07
		4121024_001	05/08/07
BHR 78	189.0583, -63.1920	4121041_001 [†]	05/08/07
B 228	235.6744, -34.1621	3011017_001	24/08/07
BHR 144	249.3750, -35.2333	3010017_001	03/03/07
L 1782-2	250.6333, -19.7272	3010010_001	03/03/07
LM 226	254.3333, -16.1461	3010012_001	06/03/07
L 1082A	313.3792, +60.2464	3010028_001	22/12/06
L 1228	314.3956, +77.6282	3011006_001	22/08/07
L 1165	331.6683, +59.0999	4121035_001 [†]	07/07/07
L 1221	337.1083, +69.0417	3010003_001	26/01/07

^a Right Ascension and Declination (J2000) at the centre of the Np aperture.

^b Observations where a second pointing with ID XXXXXXXX_002 was made immediately after the first are represented by †. All other observations are explicitly tabulated.

form in the quiescent ISM, a region probed by ice spectra towards background stars.

Limited background stars observations were first made in the 2.4 – 5 μ m wavelength range by ISO; more recently, *Spitzer* has observed many more background stars, but not in the 2.5 – 5 μ m range covering the stretching mode absorptions of H₂O, CO₂, and CO. Observing ices in this region is vital in benchmarking the inventory of ice species present at the earliest stages of star formation. Two background stars were observed by ISO: Elias 13 was observed in the range 4.20 – 4.34 μ m (focusing on the CO₂ stretching mode at 4.25 μ m (Nummelin et al. 2001)) whilst Elias 16 was observed in the ranges 2.4 – 5 μ m (Whittet et al. 1998; Gibb et al. 2004) and 14 – 19 μ m, with additional detailed studies of the CO₂ stretching mode (Whittet et al. 1998; Gerakines et al. 1999; Nummelin et al. 2001), ¹³CO₂ (Boogert et al. 2000), and potentially the N₂ stretching mode (Sandford et al. 2001). With *Spitzer*, mid IR observations were made of the same two background stars (Elias 13 (5 – 20 μ m) and Elias 16 (5 – 14 μ m)) and a third background object – CK 2 (5 – 20 μ m) (Knez et al. 2005). The CO₂ bending mode region around 15.2 μ m was investigated for a further 12 background stars across Taurus, Serpens and IC 5146 (Bergin et al. 2005; Whittet et al. 2007, 2009). CO₂ was found to exist in H₂O-poor ices in quiescent regions for the first time (Bergin et al. 2005), pointing to a formation mechanism involving CO ice. Successful ground-based studies have been carried out to observe the 4.67 μ m CO stretch towards 12 background stars (Whittet et al. 1985, 1989; Eiroa & Hodapp 1989) and the observable part of the 3 μ m water band towards 73 background stars (Whittet et al. 1988; Eiroa & Hodapp

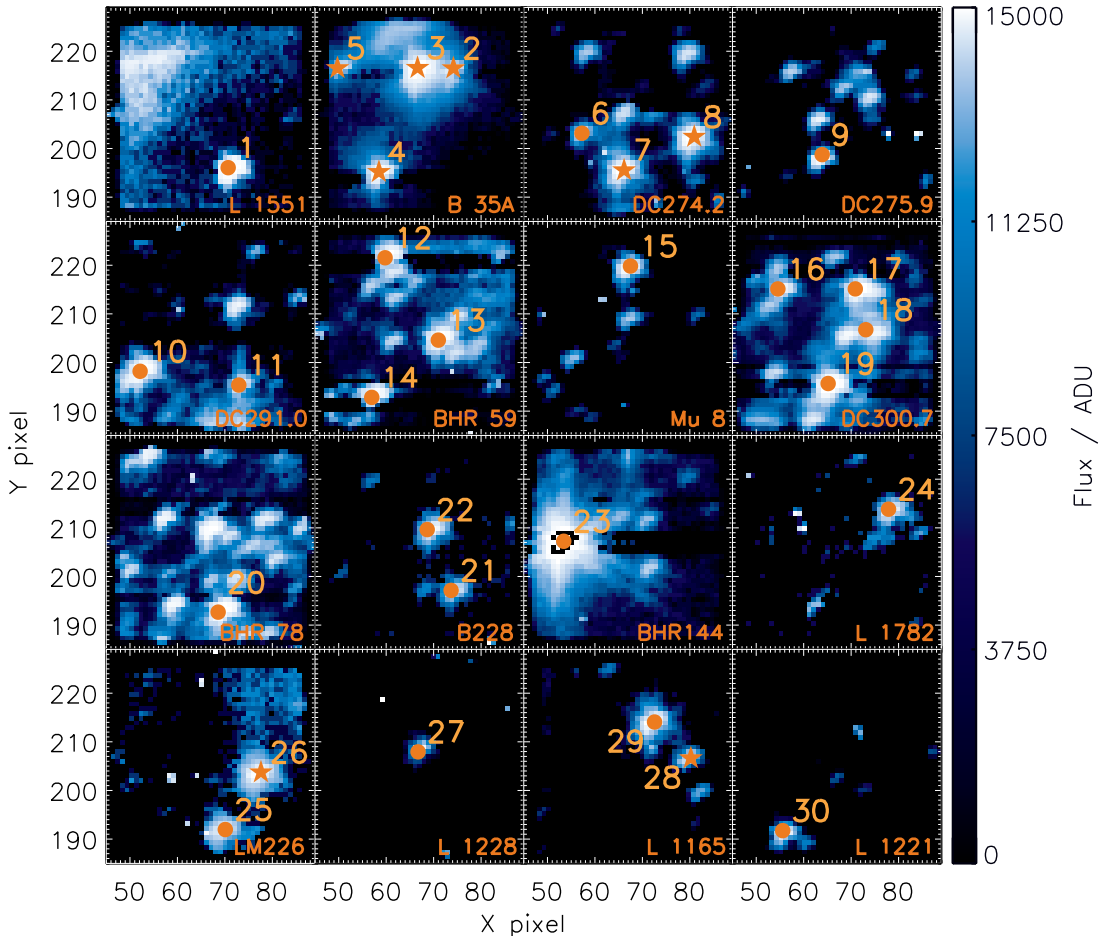


FIG. 1.— Imaging frames (at $3.2 \mu\text{m}$) for the $1' \times 1'$ grism field of view for the 16 cores that included extractable objects. X pixel is aligned with right ascension, Y pixel with declination, and the colourbar indicates the flux in each pixel. The 30 objects for which ice spectra were extracted are numbered in order of ascending right ascension; this sample includes 22 background stars (\bullet) and eight YSOs (\star). Details of each source object, including J, H, K_S photometric values and object coordinates are given in Table 3. For full details on the selection of cores and objects see § 3.2.1 and § 4.1, respectively.

1989; Murakawa et al. 2000). By combining ground-based and *Spitzer* observations, Boogert et al. (2011) quantified the ice abundances of H_2O , NH_4^+ , CH_3OH , HCOOH , CH_4 , and NH_3 towards 31 background stars (also including CO_2 abundances towards eight objects) and confirmed that little difference in the abundances of major ice species is observed between background stars and YSOs.

Most previous background star studies have been made towards Taurus and Serpens molecular clouds, with the exception of two studies of the Cocoon Nebula (IC 5146) (Whittet et al. 2009; Chiar et al. 2011), one of ρ Ophiuchi (Tanaka et al. 1990), and the survey by Boogert et al. (2011), which observed 31 background stars towards 16 isolated dense cores. Our study adds 22 background stars across a further 15 dense molecular cores to these statistics. Boogert et al. (2011) highlight that the existing studies of background stars focus on cores and cloud regions well separated from lines of sight where YSOs have been studied. To understand the subtle changes in ice chemistry as a region evolves throughout the star-formation process would require comparisons between ice spectra of these different evolutionary objects towards the same core. In three of our cores, it has been possible to compare ice column densities from back-

ground and YSO sources separated by only a few 1000 AU.

In this paper, the column densities of H_2O , CO_2 , and CO are calculated from the $2.5 - 5 \mu\text{m}$ AKARI spectra of 22 background stars and eight low mass YSOs. As the only complete spectrum of a background star in this spectral region to date is that of Elias 16 taken by ISO, this represents a significant increase in data on background stars in the NIR. In addition to H_2O , CO_2 , and CO , it was possible in certain cases to calculate the column densities of OCN^- , and CO gas-grain (Fraser et al. 2005). This large increase in data, including low flux background stars, offers much evidence about the initial conditions in quiescent molecular clouds before star formation begins. In particular, it offers clues to where ices form, and how the chemistry of different molecular species is linked in prestellar regions.

2. OBSERVATIONS

Observations were carried out between December 2006 and August 2007 using the spectroscopic mode of the Infrared Camera on AKARI (Onaka et al. 2007; Ohya et al. 2007). We observed fields of view towards 19 dense molecular clouds. Of these, 11 were part of the AKARI European Users Open Time Ob-

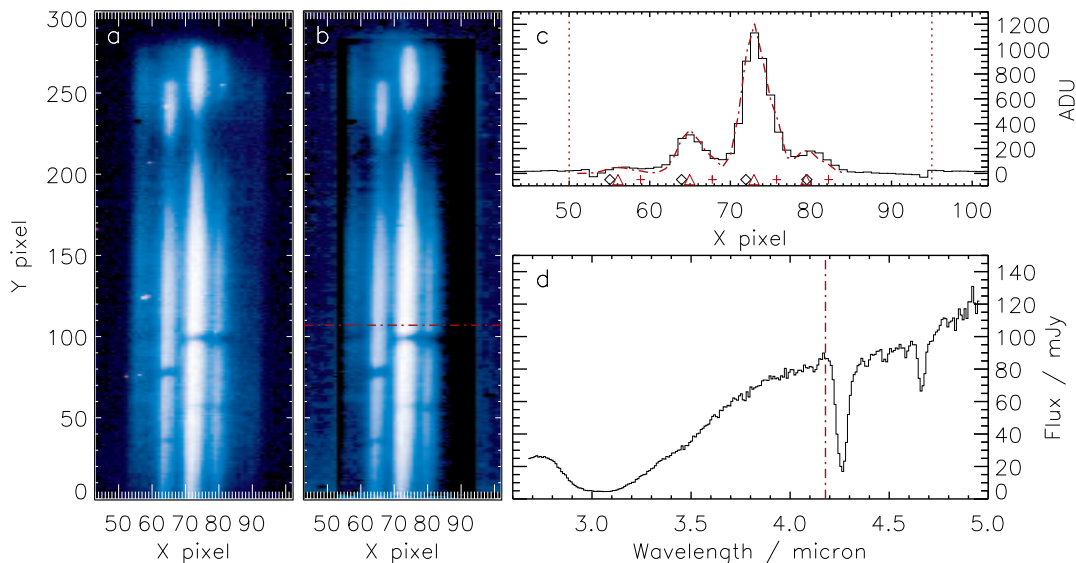


FIG. 2.— An illustration of our “AKARI Reduction Facility” pipeline, using an observation of molecular cloud B 35A. a) Single raw AKARI spectral data frame from the $1' \times 1'$ region of the NIR detector. The light from the region of sky in the $1' \times 1'$ field of view (see Figure 1) is dispersed by the grism disperser along the Y axis. The X axis remains a spatial dimension, while the Y axis is both a spatial and dispersion direction. In the Z direction (represented here by colour intensity, as per the colourbar in Figure 1) is the flux information, in Automated Data Units (ADU). b) Fully corrected data frame. Eight spectral frames have been dark-subtracted, corrected for hot and bad pixels, shifted and stacked to produce a final, corrected spectral frame. Compared with (a), in this sharper image the dispersed spectra and the ice absorptions are more distinct. Extraction of spectral data proceeds row by row along the dispersion direction; the dot-dashed (red) line represents the row $Y=108$. c) The black line shows the flux “slice” (in ADU) versus X pixel along row $Y=108$ (dot-dashed (red) line in (b)). The data are fitted with a series of Gaussian functions, as described in § 3.2. In this example, there are four objects being fitted (whose X positions are represented by black diamonds on the X axis). The central positions of the Gaussian functions in the fit are plotted as (red) triangles (on the X axis); the overall fit is superimposed as a dot-dashed (red) line. This fit well describes the data and deconvolves the overlapping flux of the four distinct objects. This process is repeated for every row in the Y direction. d) Overall final spectrum of the brightest object in this field of view. The spectrum is reconstructed from the series of flux datapoints extracted by the row fitting illustrated in (c); the datapoint produced from the fit in (c) is represented by the dot-dashed (red) line. The final spectrum on a flux-wavelength scale is produced by division by the spectral response function.

serving Programme IMAPE, a selection identified from the *c2d Spitzer* Legacy program (Evans et al. 2003); a further eight fields of view are included here from the Japan/Korea Users Open Time Observing Programme ISICE. Details of the 19 cores are given in Table 1.

In the IMAPE programme, clouds were selected by identifying those containing dense prestellar cores, a statistically large number of identifiable field stars behind the cloud, and with the proviso that no previously identified YSO candidates were in the line of sight. Two pointings were made towards each cloud, affording an improvement in the spectral signal-to-noise, and allowing for better removal of hot pixel and cosmic ray effects from the data. Details of the cloud selections in the ISICE programme, for which only single pointings were made of each cloud, are given in Aikawa et al. (2012).

The observations presented here focus specifically on data obtained with the IRC04 AKARI astronomical observing template (AOT) using the NIR grism disperser (NG). The AOT produced eight spectral frames, an imaging frame and a pre- and post-dark frame per field of view per pointing. The spectra were extracted from the Np aperture, a $1' \times 1'$ field of view with a spectral range $2.5 - 5.0 \mu\text{m}$ ($R = 120$ at $3.6 \mu\text{m}$). Imaging frames for 16 of the clouds are shown in Figure 1. The images were taken with the N3 filter ($2.7 - 3.8 \mu\text{m}$) at a reference

wavelength of $3.2 \mu\text{m}$. As is clear from Figure 1, some fields of view contain multiple objects, and as the AKARI spectroscopic mode is slitless, the spectral traces of these objects often overlap. Nevertheless, 30 individual objects were identified across these fields of view (highlighted in Figure 1) for which spectra were successfully extracted using our data reduction pipeline. The selection and classification of these individual objects are discussed later in § 3.2.1. As far as we can ascertain from the literature, ice spectra have not previously been published for any of the objects in the lines of sight observed here. Three clouds listed in Table 1 do not feature again in this paper. The field of view in DC 300.2-03.5 was too confused to enable us to extract any spectra, even though ice features may have been present; data from L 1082A and DC 269.4+03.0 were below the lower flux limit at which our pipeline functioned effectively, as discussed in § 3.2.1.

3. DATA REDUCTION

3.1. AKARI Reduction Facility (ARF)

The AKARI $1' \times 1'$ aperture was designed for point source spectroscopy of single sources and the data reduction toolkit written by the IRC team (Ohya et al. (2007), hereafter referred to as “the toolkit”) was intended to analyse such sources. In the majority of the observations in this work, there was more than one ob-

TABLE 2
SOURCE LIST.^a

Object ^b	2MASS Name	R. A. (J2000)	Dec. (J2000)	Core	J (mJy)	H (mJy)	K _S (mJy)
1 [†]	04312835+1807427	67.868103	18.128599	L 1551	0.143	1.170	2.676
2	J054429.3+090857 ^c	86.122498	9.1490002	B 35A
3	05443000+0908573	86.124964	9.1492458	B 35A	0.067	0.442	7.310
4	05443085+0908260	86.128544	9.1406136	B 35A	0.0701	0.537	5.420
5 [†]	05443164+0908578	86.131846	9.1494267	B 35A	0.393	1.320	2.370
6 [†]	09284840-5136379	142.20166	-51.610514	DC 274.2-00.4	0.086	0.373	1.880
7	09285020-5136373	142.20929	-51.610411	DC 274.2-00.4	2.380	8.000	13.600
8	09285128-5136588	142.21379	-51.616373	DC 274.2-00.4	3.280	9.080	13.900
9	09464633-5105424	146.69306	-51.095141	DC 275.9+01.9	5.530	6.260	4.580
10	10595211-6343000	164.96722	-63.716741	DC 291.0-03.5	10.300	15.700	15.600
11	10595548-6343210	164.98119	-63.722508	DC 291.0-03.5	1.150	2.320	2.370
12	11070622-6206057	166.77597	-62.101584	BHR 59	0.705	4.190	7.760
13	11071041-6206013	166.79341	-62.100358	BHR 59	0.804	5.380	11.900
14	11071034-6205345	166.79304	-62.092943	BHR 59	0.0997	1.140	6.150
15	12305017-7101331	187.70904	-71.025906	Mu 8	4.370	9.270	9.890
16	12312792-6343221	187.86635	-63.722816	DC 300.7-01.0	1.370	5.090	7.230
17 [†]	12313060-6343376	187.87753	-63.727139	DC 300.7-01.0	3.960	16.400	24.700
18 [†]	12313217-6343306	187.88413	-63.725144	DC 300.7-01.0	0.718	4.370	7.250
19	12313247-6343105	187.88539	-63.719644	DC 300.7-01.0	4.230	24.800	44.200
20	12361240-6311509	189.05177	-63.197538	BHR 78	0.488	3.030	8.500
21 [†]	15424095-3409598	235.67059	-34.166599	B 228	0.225	1.376	1.916
22 [†]	15424185-3409435	235.67439	-34.162102	B 228	0.905	3.406	4.974
23 [†]	16372876-3513588	249.36990	-35.233002	BHR 144	13.125	121.759	331.688
24 [†]	16423341-1943501	250.63921	-19.730600	L 1782-2	0.772	1.895	2.488
25 [†]	16572088-1608241	254.33701	-16.139999	LM 226	0.400	2.004	3.594
26 [†]	16572151-1608423	254.33960	-16.145100	LM 226	0.625	3.447	7.833
27 [†]	20573495+7737415	314.39560	77.628197	L 1228	1.014	4.737	7.783
28	22064175+5906156	331.67388	59.104326	L 1165	0.137	0.452	1.490
29	22064185+5906000	331.67432	59.100005	L 1165	0.216	3.470	12.300
30 [†]	22283131+6902272	337.13049	69.040901	L 1221	0.785	3.483	5.057

^a This table contains properties and extraction details of all objects with a spectrum or an upper limit. As seen in Figure 1, objects are numbered in order of ascending RA. Here, the positional and photometric properties of these objects are detailed.

^b The final spectra of all objects marked with [†] were created from only one extracted spectrum.

^c This object does not have a 2MASS ID and is thus labelled with its *Spitzer* c2d ID. Neither does it have J, H, K_S band flux values.

ject in the 1' × 1' aperture; the dispersed spectra of these objects overlapped and produced confused spectra when reduced using the toolkit. A purpose written data reduction pipeline – the AKARI Reduction Facility, hereafter referred to as “ARF” – was therefore developed by the authors to analyse AKARI NIR spectroscopic data. ARF was written in IDL, incorporating procedures taken from the IDL Astronomy User’s Library (Landsman 1993) and the Markwardt Library (Markwardt 2009). Full details of ARF are presented in Noble (2011).

The basic function of ARF is illustrated in Figure 2: the eight raw spectral data frames (Figure 2a) are dark-subtracted (using the pre-dark frame) and corrected for bad and hot pixels before being shifted and stacked. As with previously published AKARI spectroscopic studies, no flat-fielding of the spectral frames is performed, as the calibration data provided in the toolkit did not include flat fields for this region of the detector. The shift between frames is calculated by cross-correlation, for the direction perpendicular to dispersion only (X). Frames are shifted by non-integer values, as appropriate, with linear interpolation of flux to maintain absolute flux values upon stacking. Background correction is performed on the stacked frame, using a region of dark sky picked manually from the spectral aperture (Figure 2b). Objects in the field of view are identified according to their coordi-

nates, taking account of the distortion in the frame. The spectrum of each object is then extracted by fitting the grism point spread function (PSF) to the dispersed flux (Figure 2c). Extracted data are divided by the spectral response function (SRF) of the NIR detector to produce spectra on a flux-wavelength scale (Figure 2d). In general, this is a standard reduction technique, the main exception being the extraction method, described in detail below.

3.2. Extraction of spectra

3.2.1. Target object specification

Objects for extraction are introduced to ARF from target tables. Pointings that were part of the IMAPE program are a subset of the c2d *Spitzer* Legacy program and had target tables available from that program (Evans et al. 2003), including photometric data points from the Two Micron All Sky Survey (2MASS) and *Spitzer* InfraRed Array Camera (IRAC). In ARF, the c2d target lists are edited to exclude objects outside the 1' × 1' aperture and those below a threshold 2MASS K_S band (centred at 2.2 μm) magnitude of 1.19 mJy, the magnitude of the brightest isolated object (in DC 269.4+03.0) which could not be fitted with the PSF using ARF (discussed in § 3.2.3). Target tables were prepared by hand, from the 2MASS and *Spitzer* project

databases, for pointings in the ISICE program.

3.2.2. Dispersion modelling

Individual spectra are extracted by transforming the source positions from the target files to the dispersed frames, accounting for a) the distortion in the telescope optics and b) the displacement of the first order dispersion relative to the direct light position by approximately 60 pixels in the dispersion direction. The dispersion is subsequently modelled using the linear relation of $0.0097 \mu\text{m pixel}^{-1}$ with a vertical (non-dispersion, X, direction) correction of $0.00746929 \text{ pixel row}^{-1}$ to take into account the deviation of the peak position of the flux (as can be seen by inspection of Figure 2a).

3.2.3. Point spread function

The PSF of the AKARI NG disperser was calculated by fitting various combinations of Gaussian functions or Lorentzian functions to a bright point source observed in AOT04 mode (Observation ID: 5020032_001, standard star KF09T1, see Sakon et al. (2012) for further details). The best fitting combination was a double Gaussian function:

$$f(X) = \left[A_1 \exp\left\{ -\left(\frac{X - P_1}{\sigma_1} \right)^2 \right\} + 0.8A_1 \exp\left\{ -\left(\frac{X - (P_1 + 2.7)}{\sigma_2} \right)^2 \right\} \right], \quad (1)$$

where X is X pixel; A_1 the peak height and P_1 the peak position of the first Gaussian function; and σ_n the full width half maximum (FWHM) of Gaussian functions ($n = 1, 2$).

3.2.4. Running the extractor

For rows containing more than one target, a linear sum of PSFs is fitted when any targets are within five pixels of each other (in X). This is the key strength of the reduction method presented here, as this approach allows the separation of spectra which are overlapping in X, which would otherwise be discarded due to confusion. For each object in each row, the flux (in ADU) of that object at that point in its dispersion is then extracted by integrating the calculated PSF. In this way, the spectrum of each object is extracted systematically, row by row.

3.3. Flux and wavelength calibration

The SRF was generated from an observation of standard star KF09T1 in the $1' \times 1'$ aperture, with the pixel-to-wavelength relation determined by an observation of NGC 6543 in the Ns slit. The spectrum extracted from this object was compared with its calibrated model template spectrum (Cohen et al. 1999) and the response at each wavelength was obtained in units of ADU Jy^{-1} . The obtained SRF is consistent with that used in the latest IRC Spectroscopy Toolkit Version 20110114.

All extracted spectra are divided by the SRF to produce flux- and wavelength- corrected spectra, $F(\lambda)$ in units of millijansky (mJy), as illustrated in Figure 2d. The final spectrum of an object which appears in two pointings is generated by combining both spectra after division by the SRF; the two spectra are summed, and

the flux divided by two. For all spectra produced this way (not including upper limits, see § 4), the difference between the two summed spectra was less than 5 %, which was taken into account in the calculated error on the final, combined spectrum.

3.4. Error propagation

The flux error in each pixel is ± 4 ADU (Youichi Ohyama, *Private communication*). Thus the minimum error in each stacked pixel, ϵ_{min} , is calculated by:

$$\epsilon_{min} = \sqrt{n\sqrt{2 \cdot 4^2}}, \quad (2)$$

where n is the number of frames stacked, and the factor of two accounts for a contribution from subtracting the dark from each frame prior to stacking. During stacking, the standard deviation in the flux, ϵ_{sd} , is calculated. These errors are combined to calculate ϵ_{ADU} , the overall error in flux, used to weight the fit of the PSF during extraction. The error in the extracted flux, ϵ_{ext} , is the combination of the data error ϵ_{ADU} with the standard deviation of the fit. During division by the SRF, the final error on each datapoint, ϵ , is calculated by combination of the extracted flux error with the error on the SRF.

4. OBSERVATIONAL RESULTS

In total, across the 19 clouds there were 94 target objects with some 2MASS K_S band magnitude. 27 of these objects fell below the signal-to-noise threshold of ARF, defined as $K_S = 1.19$ mJy, the magnitude of the brightest isolated object for which the PSF fitting failed to converge (including all objects in DC 269.4+03.0 and L 1082A.) The confusion limit for galactic cirrus and point sources is $< 1 \mu\text{Jy}$ in N3, the $3 \mu\text{m}$ imaging filter (ASTRO-F User Support Team 2005). Four objects were only partially observed due to their position at the edge of the field of view, and were thus discounted. 33 objects were too confused to extract any spectral data because of their low flux and overlap with nearby objects, including all those in DC 300.2-03.5. The objects which were successfully extracted using ARF are detailed in Table 2; those derived from only a single spectrum are denoted by a dagger symbol (\dagger). The spectra of the 30 extracted objects are presented in Figure 3. The final spectra are shown in black, with the error on each point overlotted in grey.

Spectra were extracted across the full $2.5 - 5 \mu\text{m}$ region, except in cases where the dispersion reached the edge of the detector or where the flux from two neighbouring objects could not be resolved. For example, due to detector limitations, in Object 9 the region of the spectrum beyond $4 \mu\text{m}$ was not obtained, while for a further four objects (Objects 1, 21, 24 and 27), the higher wavelength region of the spectrum, beyond $4.5 \mu\text{m}$, was not extracted. Where unresolved overlap occurred between objects, it was possible to extract a partial spectrum, or a spectrum with some extra flux contribution, from which upper limits could be obtained on the molecular species present in the line of sight (Objects 6, 7, 8, 9, 11, 15, 16, 17, 18, 19 and 20). These objects are indicated by an arrow in Table 3 and are designated as upper limits in all figures (\downarrow).

TABLE 3
CALCULATED ICE COLUMN DENSITIES OF THE H₂O, CO₂, AND CO BANDS.^a

Object	Type ^b	N(H ₂ O)		N(CO ₂) × 10 ¹⁷ cm ⁻²		N(CO) × 10 ¹⁷ cm ⁻²		N(Minor) × 10 ¹⁷ cm ⁻²	
		× 10 ¹⁸ cm ⁻²	in CO	in H ₂ O	CO _{rc}	CO _{mc}	OCN ⁻	CO _{gg}	
1	star (M5, 19.4)	2.3 ± 0.3	< 0.6	< 0.6	
2	YSO	3.9 ± 0.3	4.7 ± 0.2	0.	6.0 ± 2.7	0.7 ± 1.0	0.	2.4 ± 0.6	
3	YSO	3.3 ± 0.1	3.1 ± 0.3	0.6 ± 0.2	3.3 ± 2.5	2.0 ± 2.9	0.	1.9 ± 0.4	
4	YSO	3.1 ± 0.1	5.0 ± 0.1	0.	0.	3.1 ± 0.9	0.1 ± 0.5	1.1 ± 1.0	
5	YSO	1.6 ± 0.3	1.3 ± 0.9	0.5 ± 0.6	0.	< 1.5	0.	0.	
6	star ↓	< 4.5	< 1.2	< 0.1	0.	< 0.6	0.	< 0.7	
7	YSO ↓	< 1.4	< 0.7	< 0.3	0.	0.	< 0.2	0.	
8	YSO ↓	< 0.8	< 2.1	0.	< 2.3	0.	< 0.1	0.	
9	star ↓	< 1.7	
10	star (K0g, 6.7)	0.7 ± 0.04	0.7 ± 0.7	0.5 ± 0.5	0.4 ± 6.9	1.2 ± 2.4	0.	0.	
11	star ↓	< 1.1	0.	< 0.3	
12	star (K0, 19.8)	0.9 ± 0.03	0.	0.5 ± 0.1	0.	0.	< 0.2	0.	
13	star (K0, 23.4)	1.4 ± 0.05	1.2 ± 0.5	0.3 ± 0.4	2.9 ± 6.9	2.3 ± 7.1	0.	< 1.0	
14	star (K0g, 41.2)	2.6 ± 0.04	3.3 ± 0.4	0.3 ± 0.3	5.4 ± 10.5	1.8 ± 20.2	0.	0.	
15	star ↓	< 0.6	0.	< 0.3	
16	star ↓	< 0.5	< 1.0	0.	0.	< 1.9	0.	0.	
17	star ↓	< 1.0	0.	< 0.7	0.	< 2.6	< 1.1	0.	
18	star ↓	< 1.1	< 0.9	0.	< 8.9	0.	0.	< 0.8	
19	star ↓	< 0.6	0.	< 0.6	< 0.8	< 0.8	0.	< 3.5	
20	star ↓	< 1.0	< 0.4	< 0.8	0.	< 1.8	0.	< 1.8	
21	star (K0, 14.0)	1.2 ± 0.1	0.	1.3 ± 0.5	
22	star (K0g, 14.6)	1.0 ± 0.1	0.	0.9 ± 0.1	0.	< 1.9	0.	0.	
23	star (K0g, 27.3)	1.5 ± 0.02	2.1 ± 0.1	0.4 ± 0.1	1.6 ± 2.4	1.7 ± 0.5	0.	< 0.6	
24	star (K0, 12.8)	0.8 ± 0.1	0.2 ± 1.0	0.6 ± 0.6	
25	star (K0, 19.2)	1.4 ± 0.2	2.0 ± 1.2	0.5 ± 1.0	3.9 ± 20.5	3.9 ± 9.2	0.	< 0.1	
26	YSO	1.5 ± 0.1	0.	1.2 ± 0.1	0.	1.7 ± 2.0	< 0.9	0.	
27	star (K0, 17.4)	1.0 ± 0.1	2.0 ± 0.6	0.4 ± 0.5	
28	YSO	2.1 ± 0.2	2.7 ± 1.4	0.1 ± 1.1	0.	0.	< 0.1	0.	
29	star (K0g, 32.7)	1.8 ± 0.04	1.5 ± 0.2	0.7 ± 0.2	2.7 ± 4.3	2.2 ± 0.6	0.	0.4 ± 0.7	
30	star (G4g, 14.9)	1.0 ± 0.1	1.3 ± 0.8	0.5 ± 0.7	0.	4.4 ± 46.4	0.	0.	

^a Column densities marked ... indicate that no fit was performed on the spectrum in the wavelength range surrounding that spectral feature. In general, this is because the spectrum was not extracted for this region - either the flux was below the extraction threshold of ARF, or the region was too confused (due to overlapping spectra) for ARF to fit that object. A value of 0 indicates that a fit was performed, and a value of 0 was returned. Only in the second case can it be concluded that this spectral feature is not present towards this object.

^b Objects from c2d target tables were categorised by the c2d team. For the objects taken from the 2MASS catalogue, the type was determined based on their J, H, K_S photometry as described in § 4.1. In addition, for background stars, the spectral type and A_V, as calculated during baseline fitting (§ 4.2), is shown in parentheses. All object marked with ↓ gave upper limits only, due to confusion in the region of the object. As baseline fitting of these objects was made with a polynomial (§ 4.2), a stellar type could not be determined for these background stars.

The H₂O band (3.0 μm) was fully extracted for all objects, including the blue wing, which is not observable from the ground. In many spectra, such as Objects 2 and 4, it is clear that the H₂O band is saturated. The error values calculated in the pipeline are the errors on the observed flux, not the errors on the absolute value of the spectral data. Where we suspect bands are saturated, we have not included any additional uncertainty on these data points. In at least 12 objects the water band is still clearly visible even though the flux is < 5 mJy (see Figure 3, Objects 1, 5, 6, 9, 21, 22, 24, 25, 26, 27, 28, 30). The absorption bands of CO₂ (4.25 μm) and CO (4.67 μm) are also clearly visible for the majority of objects.

On each spectrum in Figure 3, the IRAC photometric data points are plotted as diamonds at 3.6 and 4.5 μm. For most objects the photometric data matches the extracted flux very well. For some of the upper limits mentioned above, notably Objects 9, 11 and 16, the IRAC photometry does not exactly match the flux of the object, suggesting that there was excess light on the detector in the vicinity of the spectrum, vindicating the decision to only quote upper limits to the molecular column densities in these objects. In all cases where there is a slight

photometry mismatch, the flux of the object has been over-, rather than underestimated, supporting the conjecture that there is excess light in these fields of view. The only two examples of completely isolated objects in the dataset are Objects 27 and 30. The photometric data points for these two objects match the extracted flux within the errors.

4.1. Object classification

For further spectral analysis, it was necessary to classify each object according to whether it was a field star behind the molecular cloud (“star”) or a YSO embedded in the cloud (“YSO”). All objects in the IMAPE programme had a classification of this type preassigned by the c2d team, based on the full *Spitzer* photometric data as well as 2MASS photometry. The classification of objects in the ISICE programme was based on 2MASS photometric data. If objects satisfied:

$$1.75(H - K_S) - 0.04 \leq J - H, \quad (3)$$

they were classed as background stars; if not, they were classed as YSOs (Itoh et al. 1996; Shenoy et al. 2008). Henceforth, irrespective of the observational programme from which they are derived, the objects in this paper

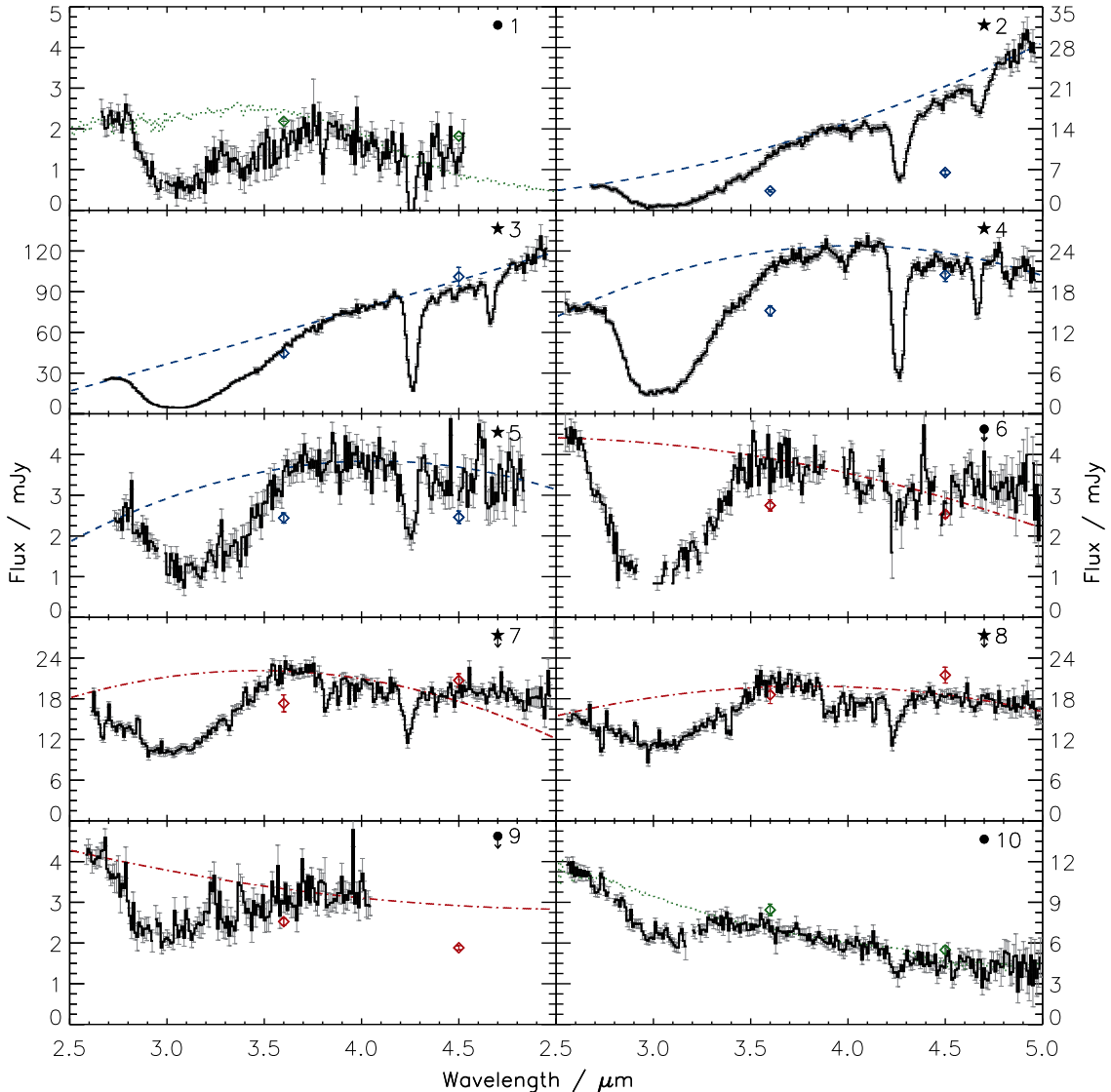


FIG. 3.— Spectra of all extracted objects on a flux scale, numbered as in Table 2. YSOs are denoted by \star , while background stars are labelled \bullet . Where spectra provide only upper limits on molecular column densities, they are labelled with an arrow. IRAC photometric data is overlotted as diamonds. In most cases, the photometry matches well with the extracted spectra. Baselines were fitted to all of the spectra (see § 4.2 for full details) and these are overlotted with the following styles: (blue) dashed for YSOs, (green) dotted for background stars, and (red) dot-dashed for upper limits.

are designated by a star symbol (\star) for YSOs, or a circle (\bullet) for background stars; in the text they are referred to as “YSO” and “star”, respectively.

4.2. Baseline fitting

To convert the observational data to spectra on an optical depth scale (most relevant for molecular abundance analysis), two different methods of baseline fitting were employed. As is typical in ice spectra extraction (Gibb et al. 2004; Öberg et al. 2011; Aikawa et al. 2012), this was either a second order polynomial (in the case of YSO objects) or a NextGen model (Hauschildt et al. 1999) (in the case of background stars), with the proviso that second order polynomials were also fitted to “upper limit” spectra, i.e. where the data were not fully extractable. These baselines are shown overlotted on each individual spectrum in Fig-

ure 3, as either a (green) dotted line (NextGen models, background stars), a (blue) dashed line (second order polynomials, YSOs) or a (red) dash-dotted line (second order polynomials, “upper limit” spectra).

The NextGen models were fitted to the background stars based on photometric data from 2MASS, IRAC and MIPS observations. Using the extinction law of Weingartner & Draine (2001), objects were dereddened along a reddening vector of 2.078 on a (J-H) vs (H- K_S) colour-colour diagram to determine their spectral type and A_V (tabulated in Table 3). Potential spectral types were defined based on where the dereddened object crossed the main sequence, giant or dwarf branches. This approach accounted well for the reddening in the 2MASS wavelength region of the spectra, but at longer wavelengths the model baselines were further reddened by a polynomial.

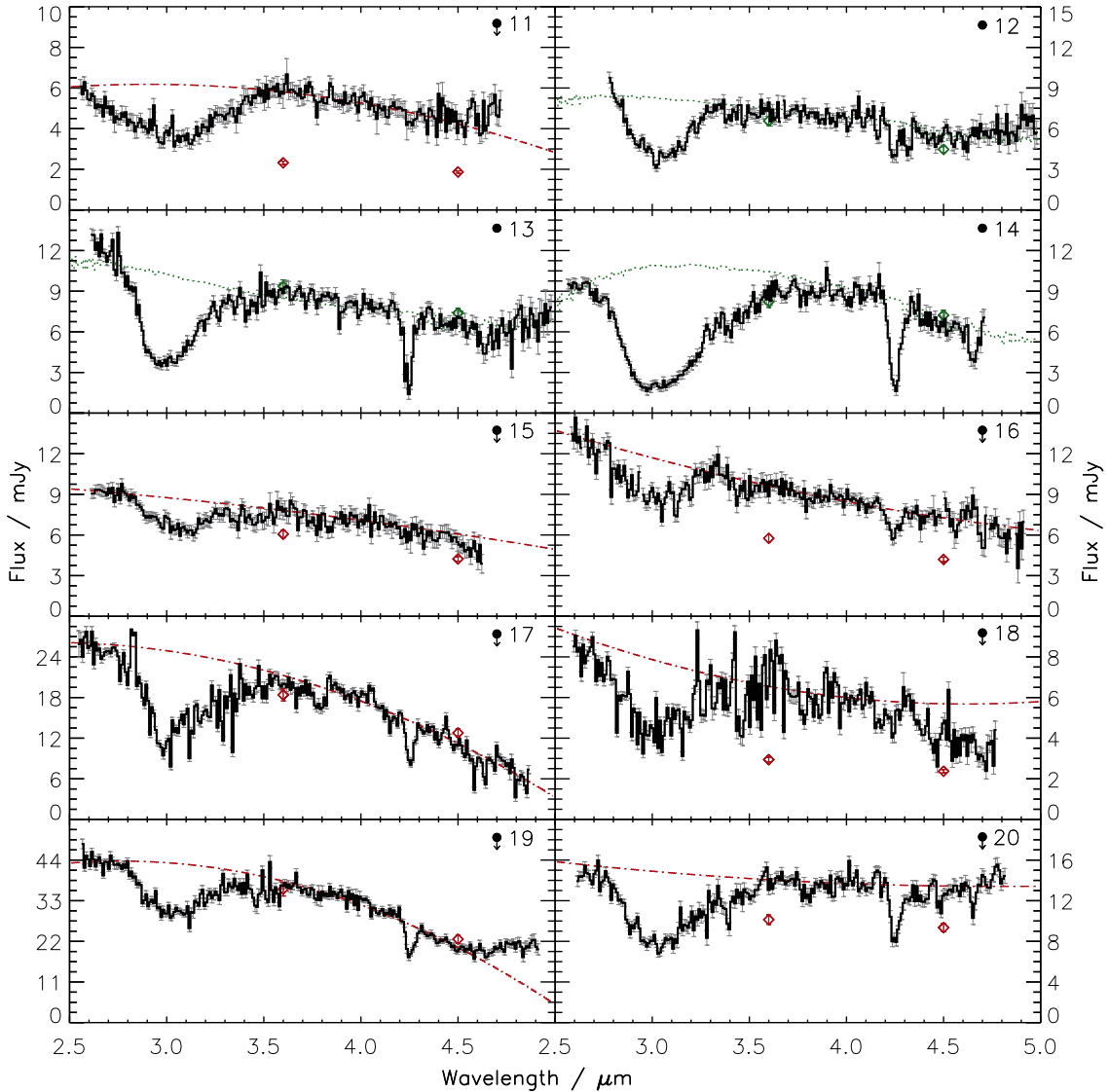


FIG. 3.— continued.

The advantage of fitting baselines with NextGen models is that the models account for emission and absorption in the stellar atmosphere. However, these models can not be used to fit YSOs as the NextGen models only include main sequence and giant stars. The continua of YSOs, (and all upper limits on background stars and YSOs) were therefore fitted by second order polynomials. Fitting regions varied slightly between the spectra, based on the position of bad pixels, but were generally $< 2.65 \mu\text{m}$, $3.85 - 4.18 \mu\text{m}$, and $> 4.75 \mu\text{m}$. The fits were weighted in favour of the blue end of the spectrum, as this region had a higher signal-to-noise ratio than the red end.

Spectra were converted to optical depth scale by:

$$\tau = -\ln(F/F_{con}), \quad (4)$$

where τ is optical depth, F is the spectral flux, and F_{con} the flux of the continuum (fitted in § 4.2). The optical depth scale spectral features are shown in Figure 4 for the $3 \mu\text{m}$ H_2O band, Figure 5 for the $4.67 \mu\text{m}$ CO band, and Figure 6 for the $4.25 \mu\text{m}$ CO_2 band.

5. SPECTRAL ANALYSIS AND DISCUSSION

The column densities of molecular species can be determined by integrating the area under their absorption bands on an optical depth scale and correcting by the optical constant for each species, using:

$$N = \int \frac{\tau d\nu}{A}, \quad (5)$$

where N is column density in molecules cm^{-2} , ν is wavenumber in cm^{-1} , and A is the band strength in cm molecule^{-1} (Gerakines et al. 1995). The specific analysis methods for H_2O , CO_2 , and CO are described in detail below. All calculated column density values are presented in Table 3.

The absorption bands of interstellar ice species are altered, with respect to those measured in the laboratory, by interaction of the incident light with the dust grains on which the absorbing ices are present. This is particularly important in the NIR where the average grain radii and absorption wavelengths are similar. Therefore

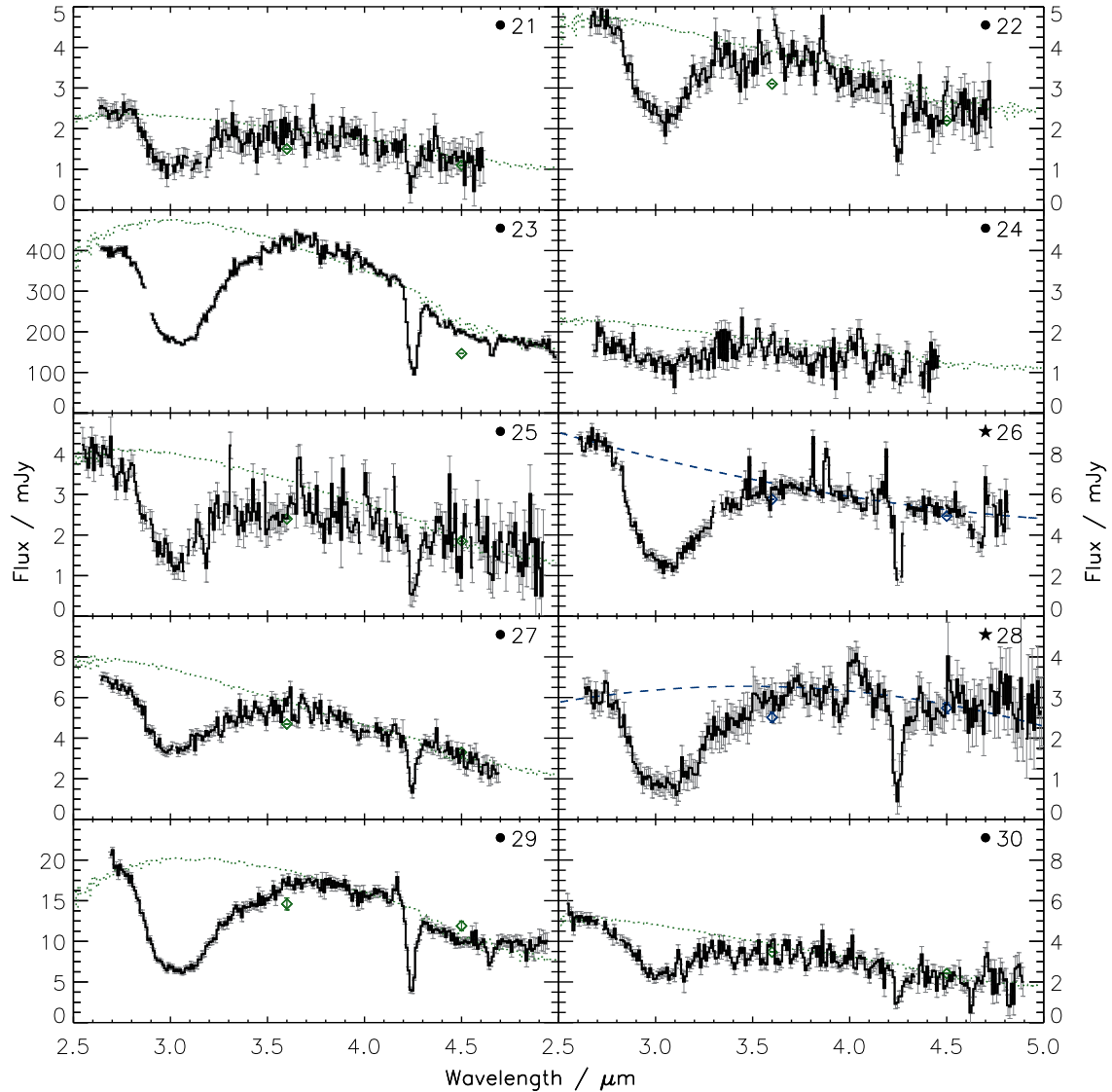


FIG. 3.— continued.

for an abundant ice species, if a laboratory spectrum is to be used to derive the column density of the ice by fitting it to the observational data, a grain shape correction must be applied. In this work, a continuous distribution of ellipsoids (CDE) model was employed. CDE is a reliable model of fractal aggregates (the likely structure of interstellar grains) and it has been successfully applied to many astronomical spectra (Tielens et al. 1991; Ehrenfreund et al. 1997; Pontoppidan et al. 2003a).

Due to the asymmetric shape of the PSF of AKARI IRC data (described above in § 3.2.3), the instrumental line profile was determined by analysis of an observation of the standard star KF09T1 in the imaging mode (IRC03). The imaging frame N3 (3.2 μm) (see Onaka et al. 2007) was chosen, and the central four pixels in the X direction were summed to produce the profile of a PSF along the Y direction, which was assumed to be the instrumental line profile.

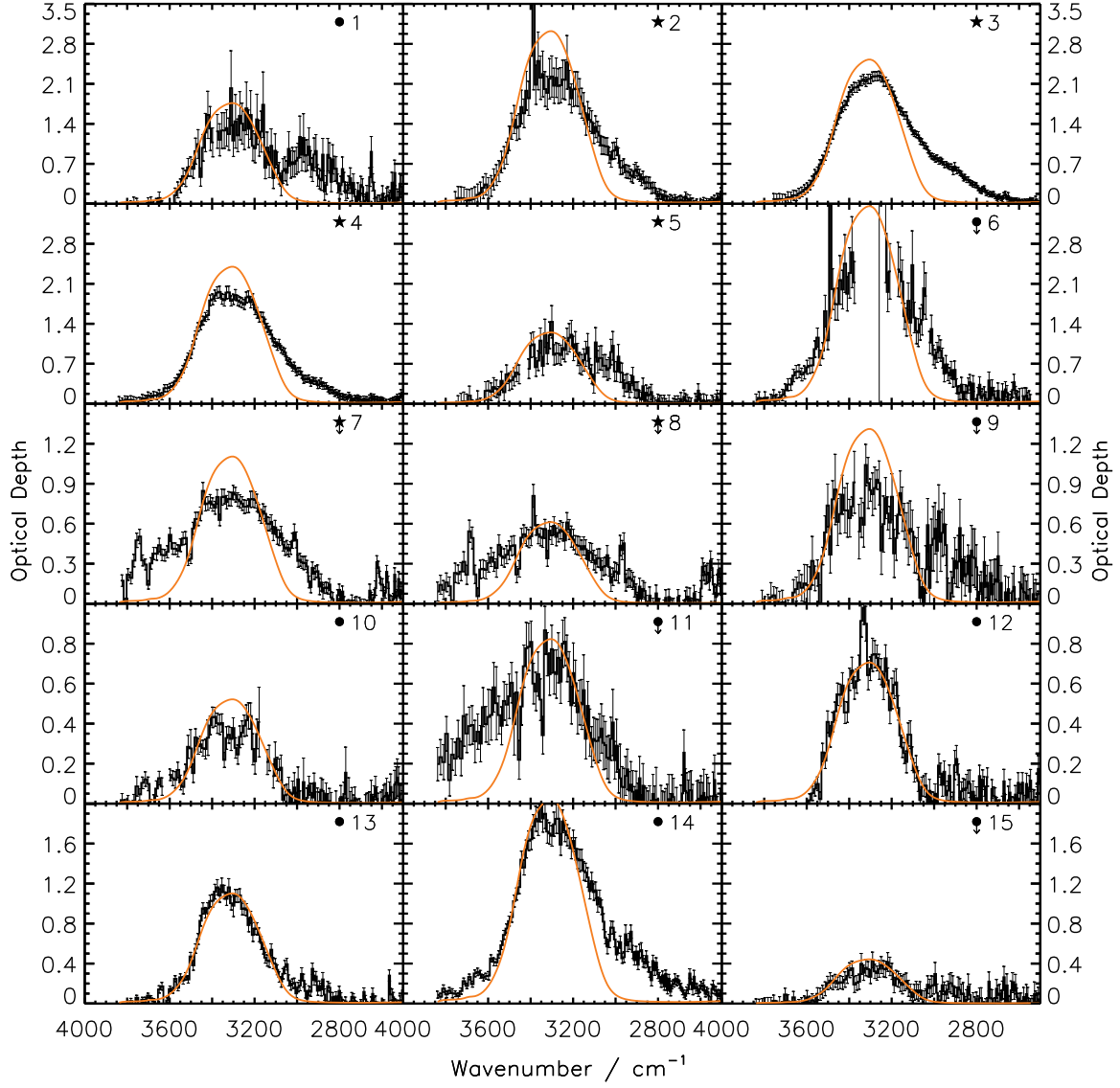


FIG. 4.— The fits of a pure non-porous H_2O laboratory spectrum at 15 K, corrected with a CDE model, the instrumental line profile, and convolved to the resolution of AKARI, to all H_2O absorption bands at $3 \mu\text{m}$ (3333 cm^{-1}). Observational data, on an optical depth scale, is plotted in black, with the fits overlotted in orange.

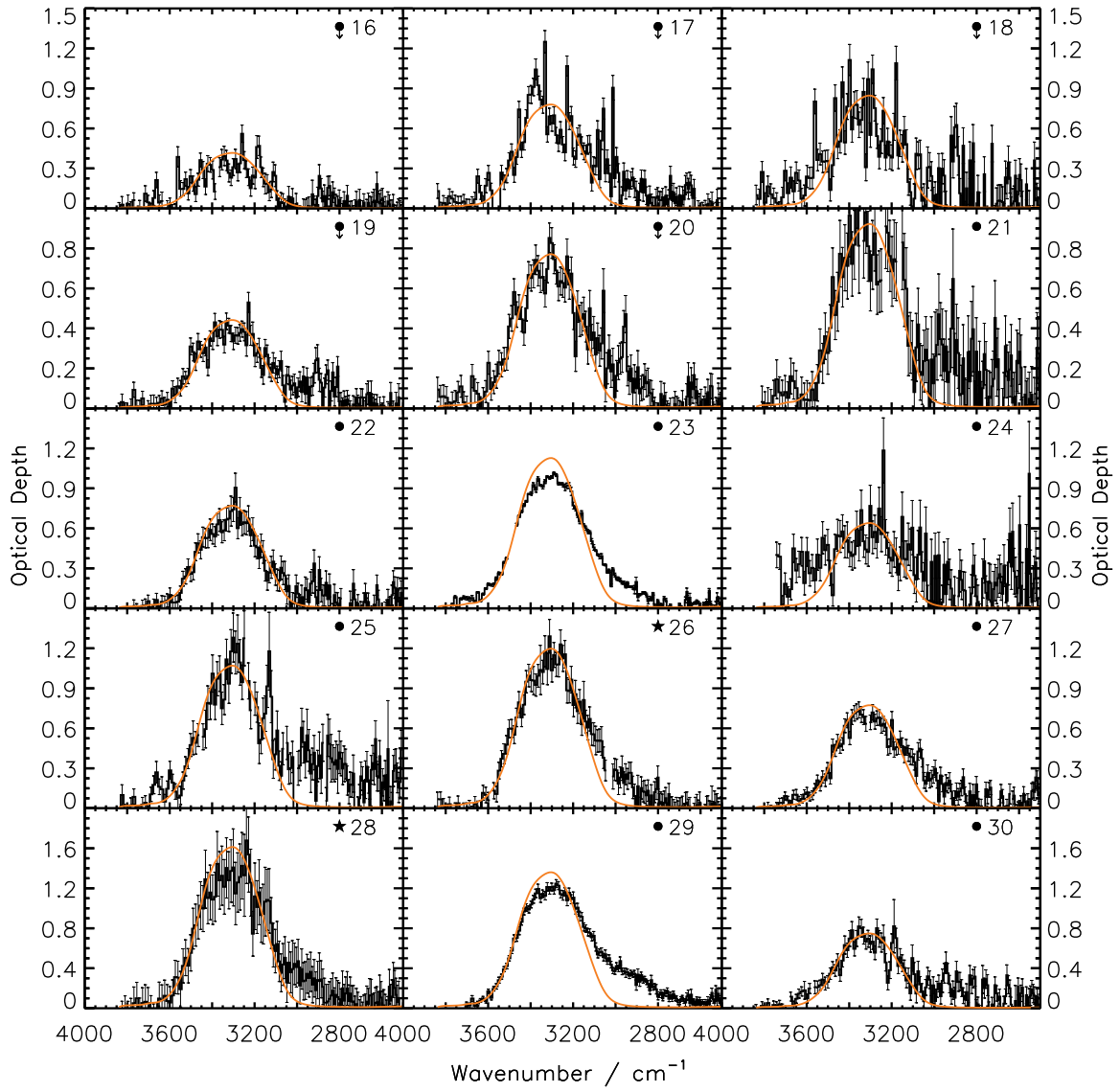


FIG. 4.— continued.

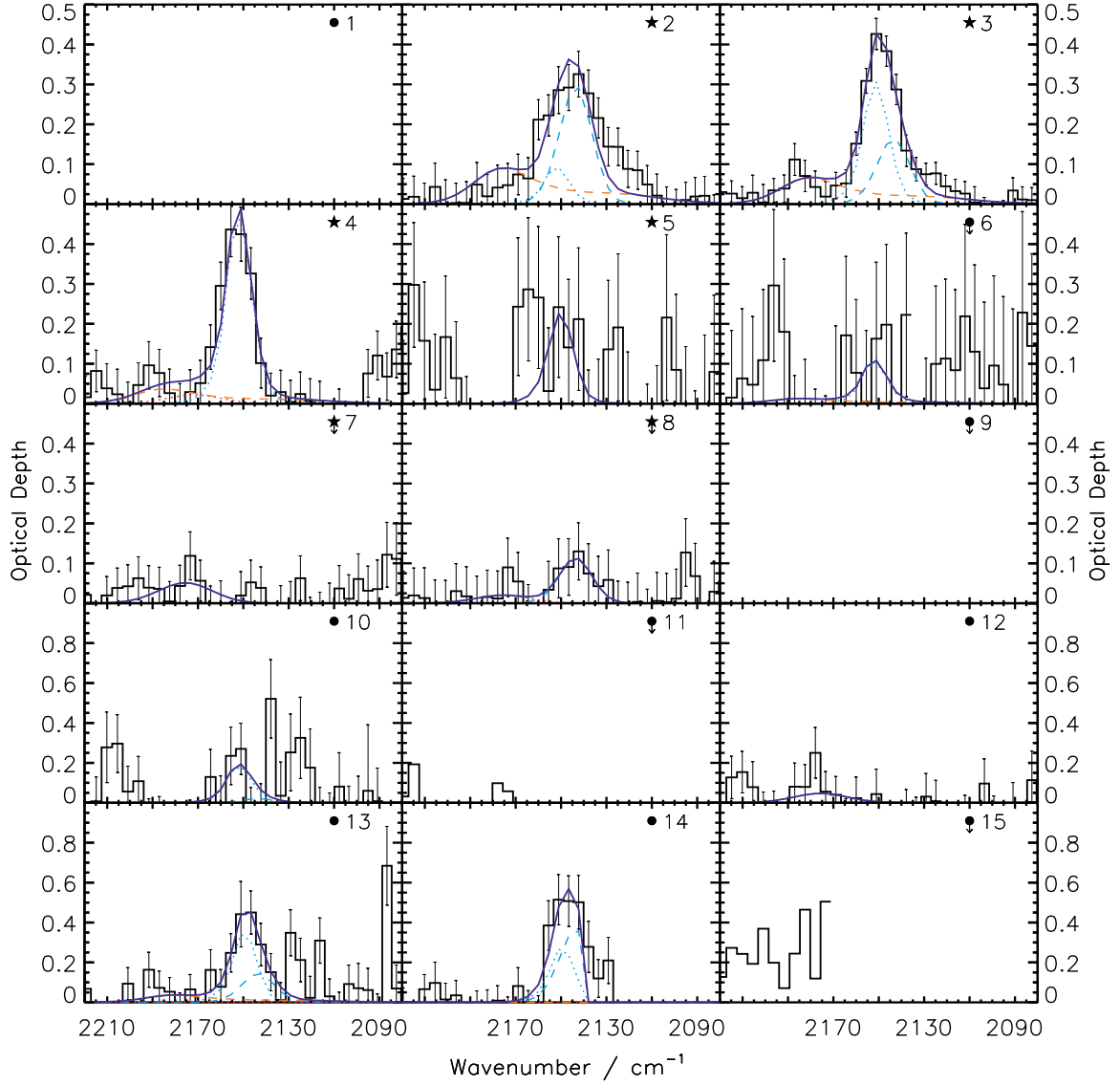


FIG. 5.— Fits to all CO absorption bands using a component analysis method. Observational data, on an optical depth scale, is plotted in black, with the fits overplotted as follows: CO_{rc} light blue dashed, CO_{mc} light blue dotted, OCN^- red dotted, CO_{gg} orange dashed, and the overall fit in dark blue (solid). CO_{mc} is CDE-corrected to account for grain shape effects, and the sum of all components is corrected for the AKARI instrumental line profile and resolution. Where there is no data in a plot, it is because no data was extracted in this region of the spectrum e.g. Object 1. Where there is only a partial data extraction, the plot is shown, but no fit was made to the data e.g. Object 11.

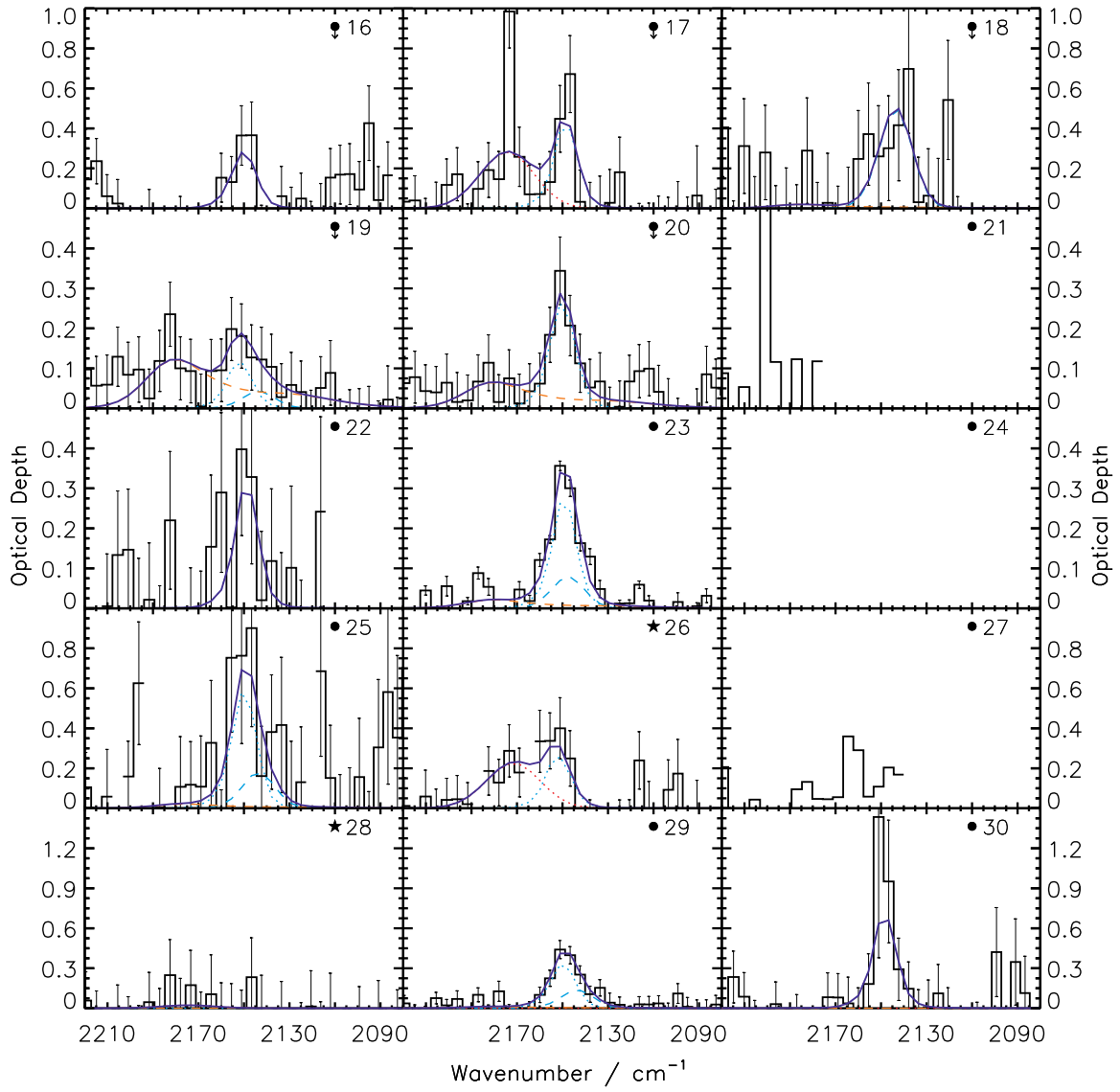


FIG. 5.— continued.

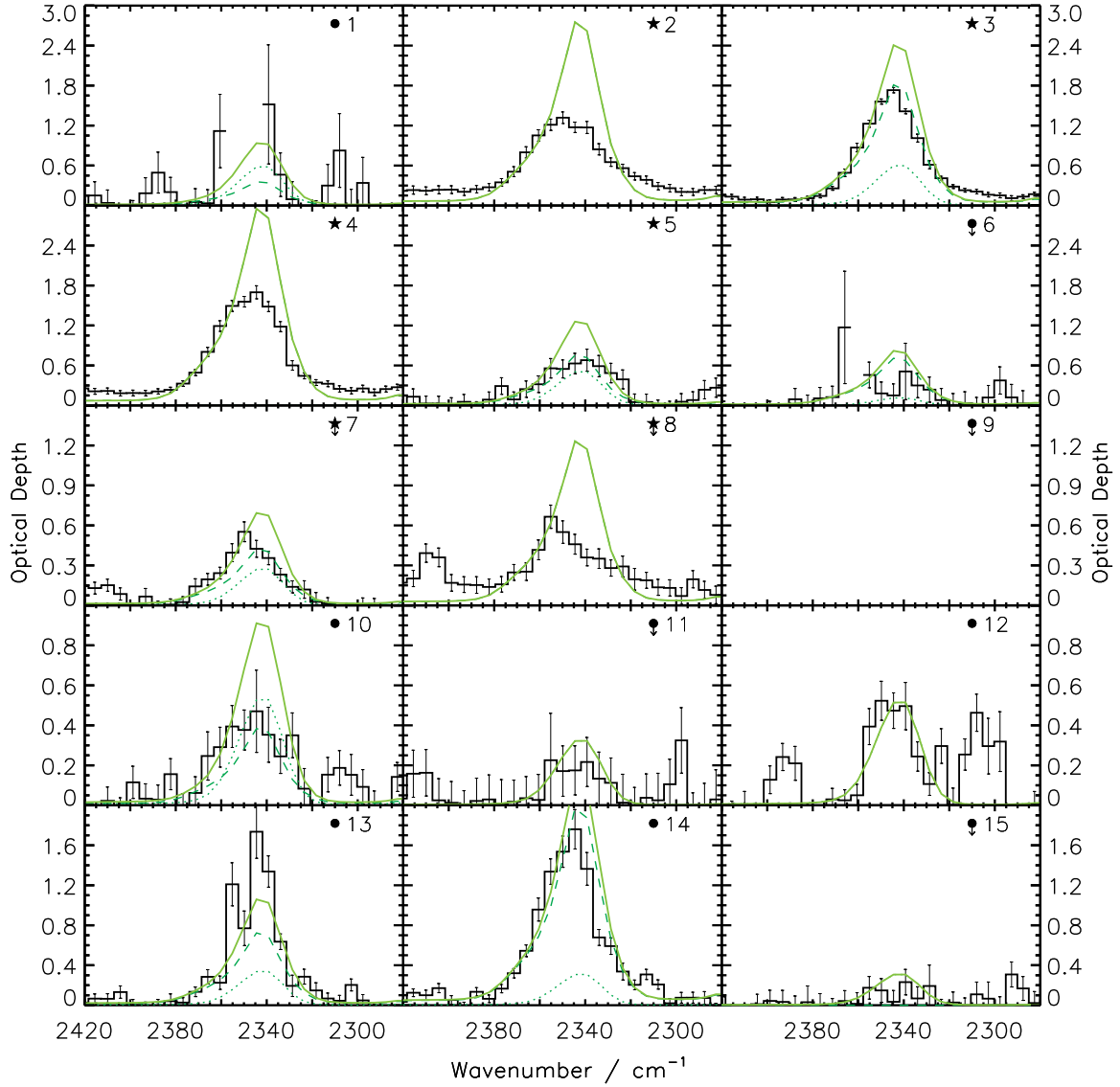


FIG. 6.— Fits to all CO_2 absorption bands using a combination of H_2O -rich and CO -rich CO_2 laboratory ices. Observational data, on an optical depth scale, is plotted in black, with the fits overplotted as follows: CO_2 in a CO -rich ice is dark green dashed, CO_2 in a H_2O -rich ice is dark green dotted, and the overall fit in light green (solid). Both components are corrected for the AKARI instrumental line profile and resolution, and CDE corrected to account for grain shape effects.

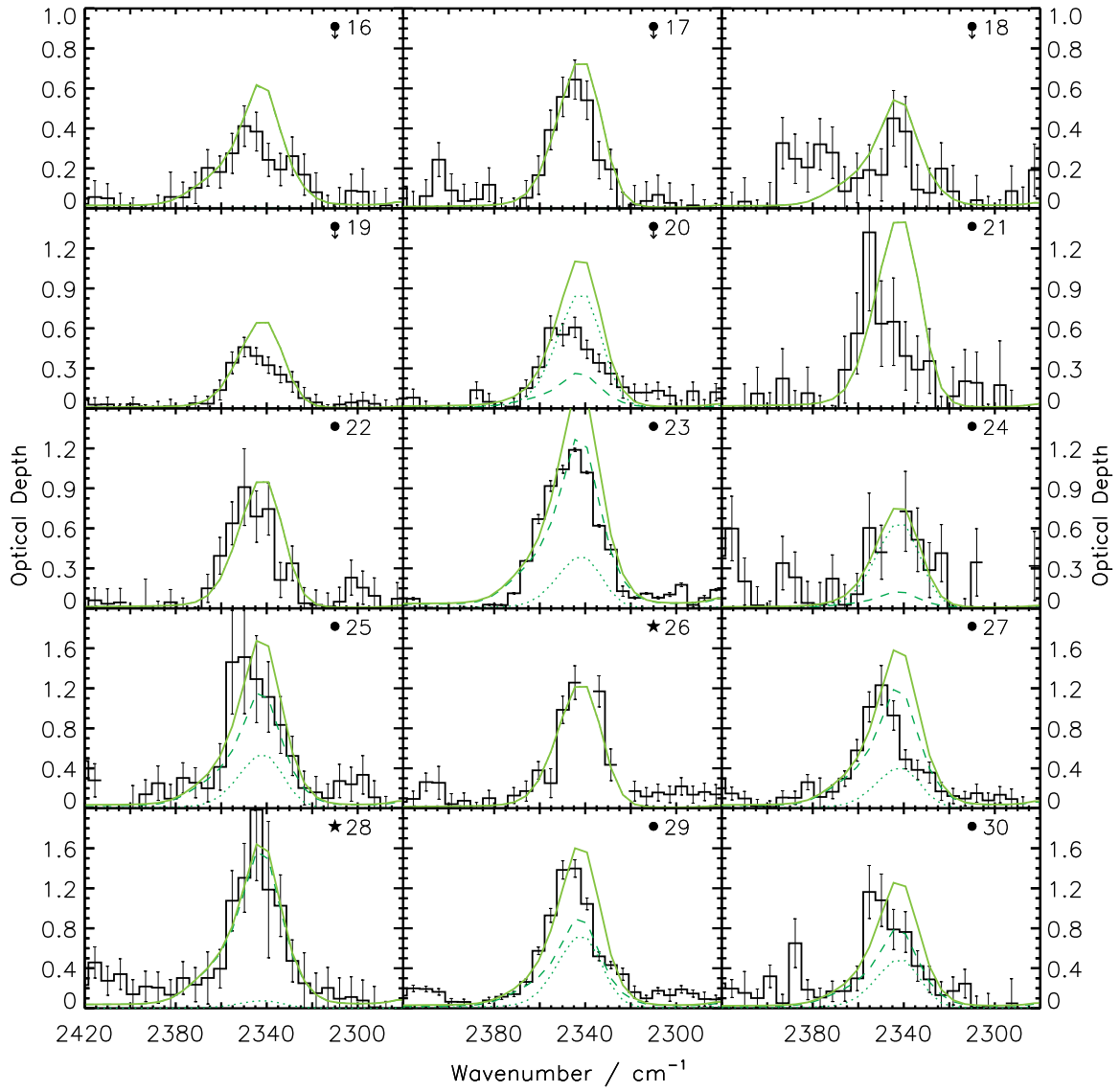


FIG. 6.— continued.

5.1. H_2O

H_2O was detected in all 30 extracted spectra, as shown in Figure 4. These spectra include a broad, smooth band extending from ~ 3600 to 2600 cm^{-1} with a steep blue wing and, in almost all cases, an extended red wing. In order to fit this H_2O absorption feature at $\sim 3\text{ }\mu\text{m}$ (3333 cm^{-1}), a CDE-corrected spectrum of H_2O was generated from a laboratory spectrum of pure H_2O at 15 K (Fraser & van Dishoeck 2004), then corrected for the instrumental line profile and resolution of AKARI. This spectrum was fitted exclusively to the blue wing of the observed H_2O data, from approximately $3600 - 3400\text{ cm}^{-1}$. Unlike the red wing, which is discussed in detail below, this region is unaffected by grain interaction effects, and is accessible here for the first time since ISO. The blue wing is also unaffected by saturation. As can be seen in Figure 4, the pure H_2O spectrum fitted the H_2O bands well in all cases.

Crystalline H_2O has a characteristic peak shape and position, and has been observed in the circumstellar disks around YSOs, where material is subject to intense irradiation from the newly formed star (Malfait et al. 1998; Honda et al. 2009). For all objects, test fits were made to examine the possibility of a crystalline H_2O component towards each line of sight, but no crystalline ice was found. A single, amorphous H_2O lab spectrum at 15 K was used to fit every H_2O absorption feature in the 30 AKARI spectra. Column densities of H_2O were calculated from the fitted laboratory spectrum using Equation 5, with $A = 2 \times 10^{-16}\text{ cm molecule}^{-1}$ (Gerakines et al. 1995), and are presented in Table 3.

Excluding those spectra yielding only upper limits, the H_2O profiles of all objects can be divided into three types, as illustrated in Figure 7. In this figure, all spectra are normalised to the maximum of the fitted H_2O band at 3300 cm^{-1} . The three distinct H_2O profiles identified were: Type 1, in which the red wing is weak compared to the absorption peak at $3\text{ }\mu\text{m}$; Type 2, in which the long wavelength feature is relatively strong, i.e. a separate shoulder; and Type 3, containing no (or very little) red contribution at all. Similar effects were noted by Thi et al. (2006), who found two H_2O band profiles in the spectra of intermediate mass YSOs in Vela: one where the extended red wing was weak relative to the H_2O ice band, and a second where it was stronger. As in Thi et al. (2006), within each subset of objects the H_2O bands show remarkably similar profiles. The question is, what are the likely origins of these profile differences? Do these profiles represent distinct physical environments, or have we, rather, sampled a continuum of red wing profiles?

Type 3 is seen only in the spectra of Objects 10 and 12, both of which are background stars and have low spectral flux ($< 12\text{ mJy}$ at all wavelengths observed). No previous observations exist of H_2O bands without an extended red wing emission. For these bands, a CDE-corrected pure H_2O spectrum appears to fully fit the observed data. Type 2 – present in the spectra of Objects 1, 13, 21, 22, 25 and 30, a sample of only background stars – appears to contain a distinct red shoulder, as opposed to the usual extended red wing. Type 1 – present in the spectra of Objects 2, 3, 4, 5, 14, 23, 24, 26, 27, 28 and 29, a mixture of YSOs and background stars – resembles

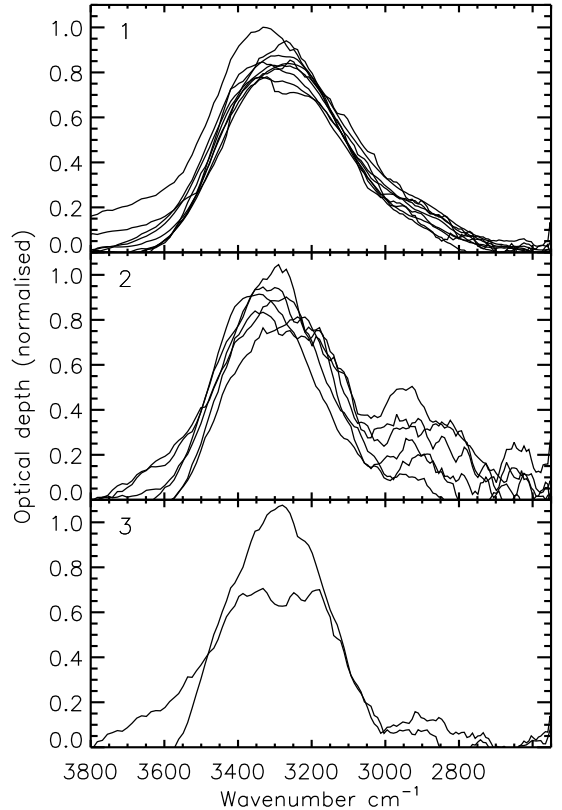


FIG. 7.— H_2O absorption band profiles for Types 1, 2, and 3. These data have been smoothed, normalised and plotted without errors, to aid comparison. It is particularly evident in this figure, from the flattened peak of the band profile, that the H_2O band is almost always saturated.

the “standard” water band observed towards many lines of sight (Gibb et al. 2004; Boogert et al. 2011). The origins of the extended long wavelength feature on the water ice band have often been debated. A number of suggestions have been made as to its origin, including: the interaction of light with dust grains (as discussed in § 5), with the depth and profile of the band changing with grain size, shape, or even as a function of ice mantle thickness (Smith et al. 1989); an absorption band at $3.54\text{ }\mu\text{m}$, attributed to the C-H stretch of methanol, CH_3OH (Hagen et al. 1980; Dartois et al. 2003); and aliphatic and aromatic C-H stretches associated with various molecular sources, including polyaromatic hydrocarbons (Onaka et al. 2011), larger organic molecules (Brooke et al. 1999) and the grains themselves (Jones 2012).

Thi et al. (2006) suggest that, although their sample is statistically limited, a strong correlation is evident between the water ice column density and the optical depth of the extended red wing at $3.25\text{ }\mu\text{m}$, concluding that the carriers of the red wing are directly related to the ice mantle. A previous study by Smith et al. (1993) also finds a strong correlation between A_v and the optical depth of the extended red wing at $3.47\text{ }\mu\text{m}$. Neither of these correlations is evident in our data. However, in comparing the average H_2O ice column densities across Types 1, 2, and 3, a clear trend emerges: the column density of H_2O ice in Type 3 sources is ~ 2.6 times lower

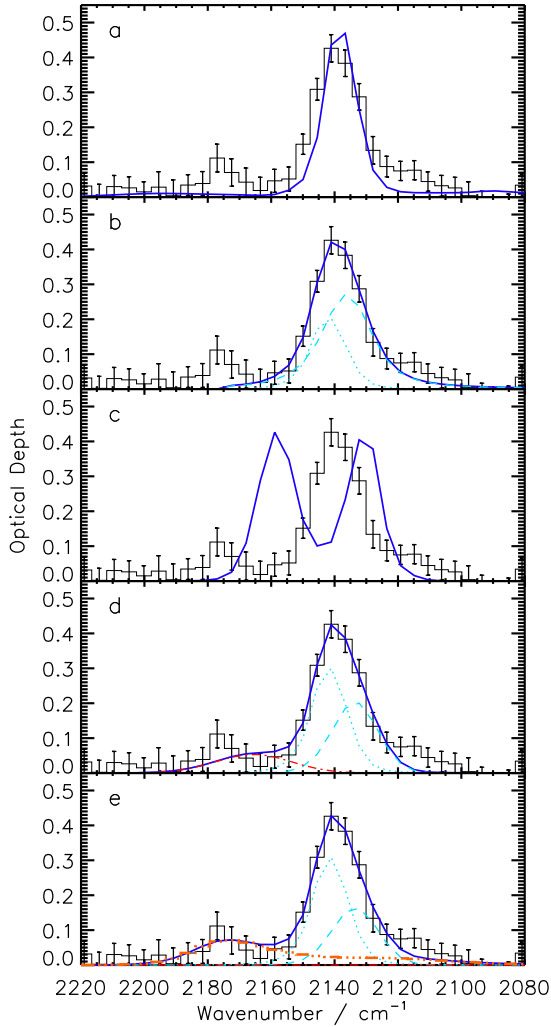


FIG. 8.— The fitting methodology for the CO absorption feature, illustrated for Object 3. Various methods were attempted before picking the final, best-fitting approach. a) a pure CO laboratory spectrum (Ehrenfreund et al. 1996); b) a combination of CO_{rc} (dotted, blue) and CO_{mc} (dashed, blue) (Pontoppidan et al. 2003a); c) a modelled CO gas phase absorption at 15 K; d) a combination of CO_{rc} , CO_{mc} , and OCN^- (dot-dashed, red) (Pontoppidan et al. 2003a; van Broekhuizen et al. 2005); e) the final fitting approach, with a combination of CO_{rc} , CO_{mc} , OCN^- , and CO_{gg} (dot-dot-dashed, orange) (Pontoppidan et al. 2003a; van Broekhuizen et al. 2005; Fraser et al. 2005).

than Type 1; Type 2 is ~ 1.5 times lower than Type 1. Given that Types 3 and 2 only contain background stars whereas Type 1 also includes YSOs it appears that the profile and depth of the extended red wing could potentially prove to be a reliable evolutionary marker. Within Type 1, whilst the band profiles are identical, the average H_2O ice column densities differ by a factor of 1.7 between the subset of YSO objects and the subset of background stars. In comparison, the ratio of average column densities between the YSO subset in Type 1 and the Type 2 background stars is 1.9. The objects of Thi et al. (2006) were all class I YSOs; the average H_2O column densities associated with their Type 1 profile (i.e. the “standard” water band) is identical to ours ($2.5 \pm 0.9 \times 10^{18}$, and $2.1 \pm 0.5 \times 10^{18}$ molecules cm^{-2} , respectively). This provides statistical evidence suggesting that the H_2O band

profile also changes with the column density of ice in a particular line of sight.

It has previously been observed that the water ice abundance ($\text{H}_2\text{O}/\text{H}_2$) in molecular cores increases with dust density at low A_V (Whittet et al. 1988), before reaching a plateau (Pontoppidan et al. 2004). Some evidence exists of a further jump in water ice abundance at densities of a few $\times 10^5 \text{ cm}^{-3} \text{ H}_2$, which has been attributed to the removal of one or more water destruction pathways (Pontoppidan et al. 2004). From our calculated column densities, it is likely that the YSOs observed in our survey probe lines of sight with densities near to the plateau, i.e. regions where grain growth and accelerated freeze-out have occurred, whereas the lines of sight towards background stars probe the density-abundance slope at lower densities, similarly to previous observations (e.g. Whittet et al. 1988). On the evolutionary path from background stars (probing low density molecular clouds or pre-stellar cores) to class I low-mass YSOs, it appears that both the grain radii and the ice mantle thickness increase. However, previous attempts to fully account for the extended red wing with this postulate have failed (e.g. Smith et al. 1989; Thi et al. 2006). Observational evidence from other ice species also points towards fundamental differences in the dust present in diffuse and dense ISM regions (Boogert et al. 2011).

As mentioned above, the H_2O band of Type 3 objects is fully fitted with a CDE-corrected H_2O ice profile, suggesting that only H_2O contributes to this absorption feature. The column densities of H_2O towards these lines of sight are relatively low, with values of 0.7×10^{18} and 0.9×10^{18} molecules cm^{-2} for Objects 10 and 12, respectively. In Type 2 objects, the main H_2O band centred at $\sim 3 \mu\text{m}$ is equally well accounted for by a CDE model as the H_2O observed towards Type 3 objects, but the column densities of H_2O are, on average, 1.8 times greater. The water ice band does not have an extended red wing, but rather a distinct shoulder redward of the H_2O band, attributed to additional molecular species present in the ice. Type 2 objects thus likely probe lines of sight towards more evolved regions of molecular cores where surface chemistry has resulted in the formation of species such as CH_3OH , or the hydrogenation of carbon on the grain surface, producing C-H bonds which absorb in this wavelength region. One further alternative, not widely discussed in the literature, is that on such lines of sight the nitrogen chemistry has evolved, forming NH_3 or at least NH_2 functional groups. The stretching modes of these transitions would appear close to the H_2O absorption (e.g. N-H stretching mode of NH_3 at $2.96 \mu\text{m}$ and amides in the region $2.70 - 3.30 \mu\text{m}$). However, for NH_3 (at least), such transitions would also be accompanied by features associated with the bending and umbrella modes of NH_3 at 6.16 and $9.00 \mu\text{m}$, respectively (Bottinelli et al. 2010); these wavelengths lie outside the NIR region probed by these AKARI observations, so no further analysis is possible here. Finally, Type 1 objects display the “standard” H_2O band profile with an extended red wing; the distinct shoulder seen in Type 2 is still likely to be present (and thus the additional carriers and molecular species remain) but is now subsumed by effects in the broad red wing of the OH stretching absorption band. The average H_2O ice column density on these lines of sight is greater than those of Types 3

and 2. However, as the fits show, this increase in column density alone cannot account for the changes in the red wing profile between Types 1, 2, and 3. Some change in the scattering properties of the ice must also occur, e.g. grain growth and mantle growth occur concurrently.

The profile of the red wing on lines of sight towards YSOs is usually attributed to grain growth, accompanied by accelerated freeze-out, which is known to occur in dense cores and regions surrounding YSOs, where the density is high enough for the freeze-out timescale to become shorter than the age of the core (e.g. Kandori et al. 2003; Román-Zúñiga et al. 2007; Chapman & Mundy 2009). It is very interesting, therefore, that Type 1 includes both YSOs and background stars, although the reasons for this have not yet been fully ascertained. One possibility is that background stars exhibiting this H₂O band profile probe lines of sight through regions of a core that are close to an existing YSO, and are thus probing ices and grains which are at a later evolutionary stage than those probed by background stars exhibiting Type 2 profiles. However, from our data this does not seem to be the case. Most of the background star subset of Type 1 are either isolated objects, or lie in fields of view containing only background stars. In the only fields of view containing a YSO and a background star (L 1165, Objects 28 (YSO) and 29, and LM226, Objects 26 (YSO) and 25), the pattern is unclear, as Object 29 is of Type 1, but Object 25 is of Type 2. Perhaps, rather, the background stars in Type 1 also probe regions which are more evolved, and are about to undergo star formation, suggesting that proximity to a YSO is not the only observational indicator of evolutionary state.

A number of studies have tried to reproduce the extended red wing profile of the H₂O band using Mie scattering with an encapsulated grain, changing grain size and mantle thickness (Smith et al. 1989; Thi et al. 2006; Dartois et al. 2002). Given that our Type 3 and 2 profiles do fit with a CDE grain shape model, we opted to continue using the CDE fitting with the Type 1 profile. Perhaps a scattering model which took into account the evolution of the ice mantle as well as grain growth would be able to more accurately model the changing profile of H₂O bands during the evolution from a molecular cloud to a YSO.

The most obvious and widely published candidate molecule to account for the H₂O band shoulders in Types 2 and 1 is CH₃OH. It has previously been observed towards multiple lines of sight including both low mass YSOs and background stars (Brooke et al. 1999; Pontoppidan et al. 2003b; Boogert et al. 2011). As the focus of this article is the analysis and quantification of the H₂O, CO₂ and CO ice absorption features, further analysis of the H₂O red wing was not performed. This issue will be addressed in a future article (Suutarinen et al, in preparation).

5.2. CO

The original aim of these observations with AKARI was to determine the relative column densities of H₂O, CO₂, and CO ices, with a view to mapping ices across molecular clouds. Given the low spectral resolution of AKARI, it was not anticipated that the absorption features would be fully resolved, and thus a component fitting method was not envisioned. However, the profiles

of the CO bands observed are well enough resolved that fitting components is viable.

The fitting methodology for CO was developed by consideration of various possible methods, the most crucial of which are illustrated in Figure 8. The primary CO feature (2160 – 2120 cm⁻¹) contains only nine or ten data points, while the AKARI instrumental profile contains 10 data points. These data are thus below the Nyquist limit for data sampling, and we expect the CO feature to be undersampled. A single component fit of pure CO to the primary CO feature using a lab spectrum (with applied CDE model, AKARI instrumental profile and resolution correction) (Figure 8a) was discounted as the wings were poorly fitted. A two component fit of pure CO and CO in a water environment (middle component, CO_{mc}, and red component, CO_{rc}, Pontoppidan et al. (2003a)), similar to that first described by Tielens et al. (1991), well described the main CO feature, especially the wings (Figure 8b), with the reduced chi-squared statistic improving for 74 % of spectra. However, it did not account for the 2160 – 2180 cm⁻¹ feature, nor the slight excess in the red wing of the CO feature. Previous AKARI observations showed that gas phase CO rovibrational lines might also be present concurrently with the CO ice feature (Aikawa et al. 2012) at least on lines of sight towards the edge-on disks they observed. At the AKARI resolution, these gas phase lines are not resolved, but the possibility of major gas phase CO features in absorption was considered, and rejected, based upon a series of model gas phase spectra, one of which is shown in Figure 8c. Clearly the gas phase features peak where the ice features do not, even at the AKARI resolution, and they cannot account for the extended red wing on the AKARI CO ice features. We conclude that there is very little, if any, gas phase CO contribution in our spectra, and do not include a gas phase component in our fit. The feature between 2160 – 2180 cm⁻¹, which is usually attributed to OCN⁻ (e.g. Pontoppidan et al. 2003a), is included in the overall fit for completeness, although the minor components contributing to this feature are not discussed further in this work. In our spectra, the feature can usually only be fully accounted for by including both an OCN⁻ component and the so-called CO_{gg}, CO gas-grain, feature (Fraser et al. 2005), as illustrated by van Broekhuizen et al. (2005). CO_{gg} represents gas phase CO that chemisorbs directly to the bare grain surface during or before formation of the underlying H₂O ice mantle (Fraser et al. 2005). As can be seen from Figure 8d, the OCN⁻ feature alone is not able to fully complete the fit and so, as illustrated in Figure 8e, we use both components here. The inclusion of the secondary feature (2160 – 2180 cm⁻¹) to the fit makes no difference to the calculated CO column densities for all spectra from which CO values were calculated (nor for 80 % of upper limit values).

Ultimately, our CO ice band fitting was based on a modified version of the well-established four component analysis of Pontoppidan et al. (2003a). In our analysis, CO_{rc} is replaced by a Gaussian calculated from laboratory data (Cottin et al. 2003), but CO_{mc} is retained as in Pontoppidan et al. (2003a) (a CDE-corrected Lorentzian at 2139 cm⁻¹). The third CO component from Pontoppidan et al. (2003a) is omitted,

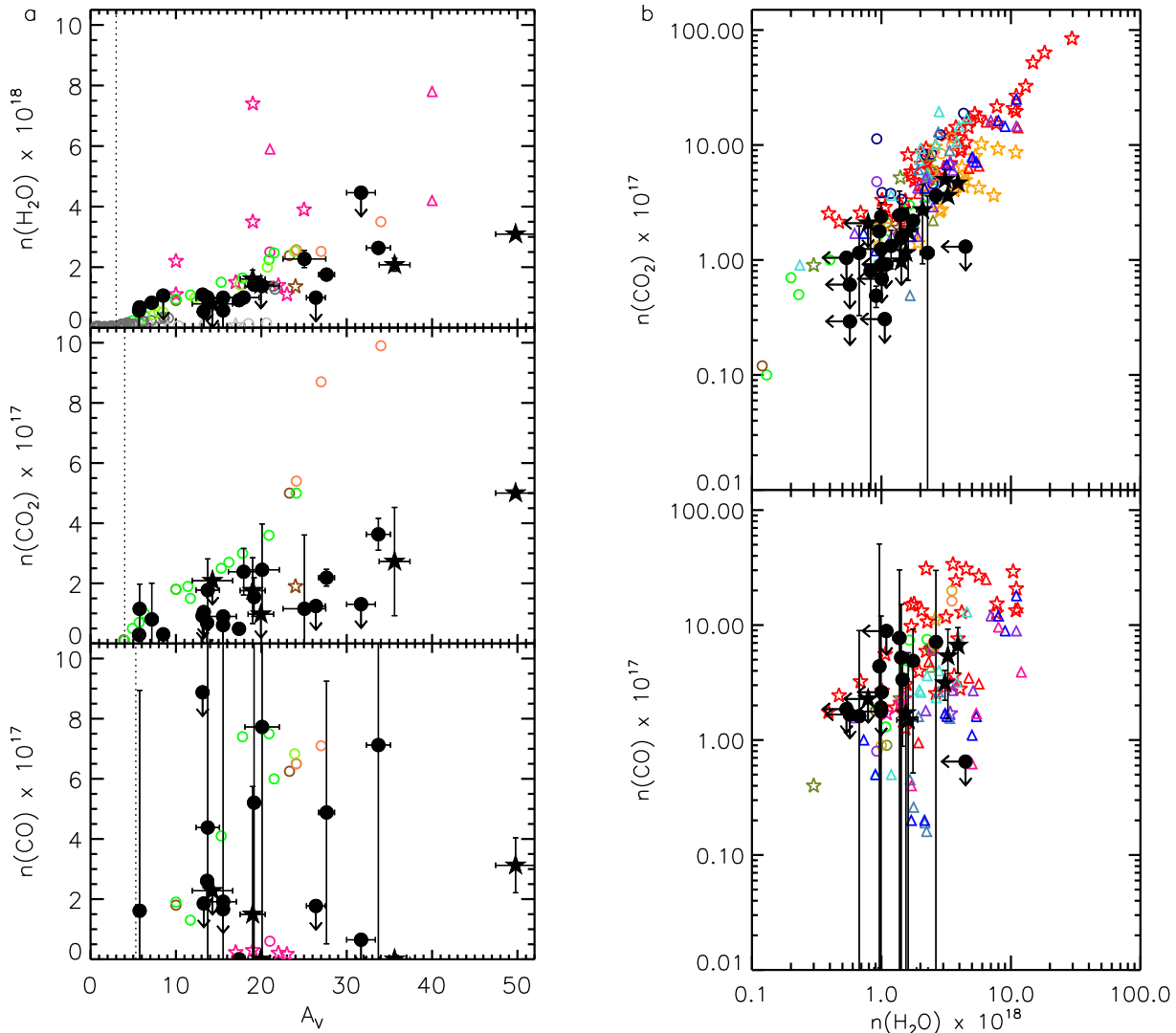


FIG. 9.— Correlation plots of calculated H_2O , CO_2 , and CO column densities with extinction. In this, and all subsequent, correlation plots, data calculated in this work are plotted as follows: background stars are plotted as filled circles (\bullet) and low mass YSOs as stars (\star), with upper limits designated by arrows (\downarrow). Also plotted, as empty symbols, are literature values for completeness, plotted as triangles (Δ). In the electronic version, different studies are plotted in different colours, as defined below. Plot a) Column densities of H_2O , CO_2 , and CO plotted against A_V . In each plot, the dotted line represents the critical A_V value calculated by previous studies. Plot b) Column densities of CO_2 and CO plotted against H_2O . The literature values are taken from: light grey (Whittet et al. 1988), royal blue (Gerakines et al. 1999), dark grey (Murakawa et al. 2000), olive green (Nummelin et al. 2001), violet (Gibb et al. 2004), pink (van Broekhuizen et al. 2004), gold (Knez et al. 2005), brown (Bergin et al. 2005), green (Whittet et al. 2007), red (Pontoppidan et al. 2008), orange (Zasowski et al. 2009), coral (Whittet et al. 2009), turquoise (extragalactic, Shimonishi et al. 2010), navy blue (Boogert et al. 2011), blue steel (extragalactic, Oliveira et al. 2011), bright green (Chiar et al. 2011).

not because it is not necessarily present, but because, given the AKARI resolution, there is no need to add additional components to a fit, where two components suffice. That only two components are required to fit the main CO feature (CO_{mc} and CO_{rc}) supports our assertions that ARF, and in particular the stacking method, was appropriate for analysis of these data. The $2160 - 2180 \text{ cm}^{-1}$ feature, (the fourth component in the Pontoppidan et al. (2003a) method), was fitted by a Gaussian derived from laboratory OCN^- spectra by van Broekhuizen et al. (2005). In addition, a laboratory spectrum of CO gas chemisorbed on a zeolite surface ($(\text{CO}_{gg}$, Fraser et al. 2005)) was added to the model, to fit the outlying absorption feature centred at 2175 cm^{-1} .

CO_{mc} is CDE corrected to account for grain shape effects, and the sum of all components is corrected for the AKARI instrumental line profile. One key element of the multi-component fitting in Pontoppidan et al. (2003a) is that all the components are used to fit all the observed spectra, changing only the relative intensities of each component from one line of sight to another. This is the premise we also adopt here.

The fits of CO are presented in Figure 5. Where there is no data in a plot, it is because no data was extracted in this region of the spectrum (e.g. Object 1). Where there is only a partial data extraction, the plot is shown, but no fit was made to the data (e.g. Object 11). Interestingly, it is very clear from Figure 5 that in at least

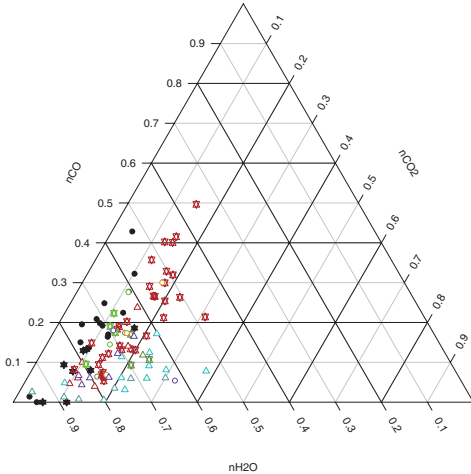


FIG. 10.— Ternary plot of the relative calculated column densities of H₂O, CO₂, and CO. For each line of sight, the sum of all three axes is 1. As before, in the electronic version of the data labels are coloured as follows: olive green (Nummelin et al. 2001), violet (Gibb et al. 2004), gold (Knez et al. 2005), green (Whittet et al. 2007), red (Pontoppidan et al. 2008), turquoise (extragalactic, Shimonishi et al. 2010), blue steel (extragalactic, Oliveira et al. 2011). In this plot, low mass YSOs are plotted as sextiles (*).

two objects – Objects 4 and Object 20 – the CO ice main peak is fully described by a single pure CO component (CO_{mc}). In fact as Table 3 shows, up to nine objects fit into this category. Conversely, in Objects 8 and 18, the CO ice is fully fitted by only the CO_{rc}. However both these objects provide only upper limits on the CO ice column densities, and the identification of a single CO ice component is much less compelling than for Objects 4 and 20. Given that CO ice is formed in low temperature cores, where CO gas critically freezes-out as densities increase, it is perhaps not surprising to observe objects with only pure CO ice present. As the temperature of a core increases (usually due to the formation of a YSO), this pure CO ice is expected to either desorb or migrate into the pores of the underlying water ice, giving rise to the CO_{rc} (Collings et al. 2003a). In the laboratory it is only possible to detect the spectral feature associated with the CO_{rc} at elevated temperatures (Collings et al. 2003b), but it seems unlikely that the lines of sight probed here are particularly warm. The origins of the CO_{rc} therefore remain debatable, as illustrated recently by Cuppen et al. (2011).

The column density of CO for the pure component, CO_{mc}, is calculated by:

$$N(\text{CO}_{mc}) = 6.03 \text{ cm}^{-1} \times \tau_{max,mc} \times A_{bulk}^{-1}, \quad (6)$$

where $A_{bulk} = 1.1 \times 10^{-17} \text{ cm molec}^{-1}$ is the band strength of the bulk material, and $\tau_{max,mc}$ is the optical depth at maximum absorption (Equation 3, Pontoppidan et al. (2003a)). $N(\text{CO}_{rc})$ and $N(\text{OCN}^-)$ are calculated using Equation (5), with band strengths $A_{rc} = 1.1 \times 10^{-17} \text{ cm molec}^{-1}$ (Gerakines et al. 1995) and $A_{OCN^-} = 1.3 \times 10^{-16} \text{ cm molec}^{-1}$ (van Broekhuizen et al. 2004). The column density of

the CO gas-grain population is calculated by:

$$N(\text{CO}_{gg}) = 1.07 \text{ cm}^{-1} \times \tau_{max,gg} \times A_{bulk}^{-1}, \quad (7)$$

where $A_{bulk} = 4.0 \times 10^{-19} \text{ cm molec}^{-1}$ is the band strength of the bulk material (Fraser et al. 2005), and $\tau_{max,gg}$ is the optical depth at maximum absorption. All column densities calculated for CO_{rc}, CO_{mc}, OCN⁻, and CO_{gg} are presented in Table 3. It should be noted that A_{bulk} is calculated based upon laboratory spectra of a particular ice, using estimations for the parameters of ice thickness and number of molecules on the surface. If astrophysical ices differ in mixture or concentration, the relationship between optical depth and molecular abundance will change, and thus the relative concentration of one component to another will differ with respect to the values calculated here. This caveat holds for any interstellar ice column density analysis.

OCN⁻ was believed to be formed around YSOs, based upon upper limits established by studies of background stars (Whittet et al. 2001) which suggested that OCN⁻ is not found in quiescent clouds. However, more recent studies have revealed stricter upper limits on OCN⁻ towards background stars probing quiescent regions (Knez et al. 2005). As is evident with reference to Table 3, an OCN⁻ component was fitted towards very few lines of sight (five YSOs and two background stars, all but one of which were upper limits).

5.3. CO₂

The CO₂ stretching mode is a very deep absorption feature and therefore it can easily become saturated; it is suspected that this is the case here. A second challenge in fitting the CO₂ ice region at the AKARI resolution limits, is that across the whole feature there are only 18 – 19 data points, which means that the line is not necessarily fully sampled, and potentially that the observed peak position in the spectrum is not coincident with the actual peak absorption. This also means that it is impossible to fit the CO₂ bands with the wings only, unlike in the case of H₂O. Furthermore, like the CO₂ bending mode at 15.2 μm, the stretching mode of CO₂ is very sensitive to the ice mixture, temperature, and other properties, as demonstrated by a number of laboratory experiments (e.g. van Broekhuizen et al. 2006). Consequently, when fitting the CO₂ stretching mode there are a wide range of potential fitting parameters and degenerate solutions.

It is clear from previous AKARI studies that quantification of CO₂ abundances using AKARI spectra is challenging. Shimonishi et al. (2010) calculated the CO₂ abundance towards massive YSOs in the Large Magellanic Cloud as ~ 36 % relative to H₂O using a curve of growth method. In observations of CO₂ ice on lines of sight towards edge-on disks, Aikawa et al. (2012), determining abundances from the integration of a fitted laboratory spectrum, found CO₂/H₂O ratios broadly consistent with those published previously (e.g. Pontoppidan et al. 2008). Of course, such differences may be wholly attributable to the types of objects observed – extragalactic YSO sources in the case of Shimonishi et al. (2010); ice in edge-on YSO envelopes and disks in the case of Aikawa et al. (2012), where the collapse may have occurred so rapidly that less CO freeze-out led to less CO₂ formation. In the two cases

cited, CO₂ column densities were calculated using a single laboratory component or a curve of growth method. In this work, we will fit our data with a two component model, to make better fits to the CO₂ stretching absorption.

Given that previous detailed *Spitzer* observations have established, from the bending mode feature, that CO₂ exists in two environments (a water-rich ice and a carbon monoxide-rich ice) towards YSOs (Pontoppidan et al. 2008) and background stars (Knez et al. 2005; Boogert et al. 2011), it was decided to fit the feature with two laboratory spectra: a CO₂:H₂O 14:100 ice at 10 K (Gerakines et al. 1995) and a CO₂:CO 1:1 ice at 15 K (Fraser & van Dishoeck 2004). A Kramers-Kronig analysis (Bohren & Huffman 1983; Ehrenfreund et al. 1997), followed by a CDE grain shape model and the AKARI instrumental line profile were applied to both laboratory spectra before fitting the peak (excluding the central four data points, as they might not fully describe the maximum absorption). From Figure 6, it is clear that the strategy fits the observed data well, including the peak. Where there is saturation of the CO₂ band, this is also reflected by the fitting, with the wings well described but the final fit illustrating the significant undersampling in the AKARI data. The reduced chi-squared statistics were improved for all but one spectrum (97 %) when comparing a two-component fit to fitting a single laboratory spectrum, further justifying our choice of fitting methodology.

Column densities were calculated using Equation (5) with $A = 7.6 \times 10^{-17}$ cm molecule⁻¹ (Gerakines et al. 1995), and are presented in Table 3. For the YSOs in our sample the values obtained are commensurate with those previously reported for low-mass YSOs (Pontoppidan et al. 2008; Aikawa et al. 2012); the column densities for the lines of sight towards background sources are generally lower, as found in previous studies (e.g. Knez et al. 2005; Boogert et al. 2011).

6. ASTROCHEMICAL IMPLICATIONS

As explained in the introduction to this article, a key aim of these observations was to explore the links between H₂O, CO₂, and CO ice column densities, and to test the chemistry relating these species. Figure 9a shows the calculated column densities of the three most abundant solid phase molecular species, H₂O, CO₂, and CO, plotted against visual extinction, A_V . The lowest A_V of any object in these AKARI data is 5.68.

Our results clearly follow the trends established by previous observations. Both the H₂O and CO₂ column densities increase with A_V , commensurate with the previously calculated critical A_V values of ~ 3 and ~ 4 , respectively, although such low extinctions were not probed in this subset of AKARI observations. For both H₂O and CO₂ we would expect an increase in ice column density with A_V ; more dust equals, on average, more ice.

Conversely, in Figure 9a, there is no clear relationship between CO and A_V . There is a much greater spread in CO values compared to those seen for H₂O and CO₂ in the panels above. CO is known to form in the gas phase and freeze-out onto the grain surface above a critical A_V (which has been estimated, variously, as ~ 3 in Serpens (Chiar et al. 1994), ~ 5 in Taurus (Whittet et al. 1989), and ~ 11 in ρ Ophiuchi (Shuping et al. 2000)), but not

necessarily as a function of dust density, as the CO gas density is more critical (Pontoppidan et al. 2003a). Towards one line of sight, CO is observed in the solid phase at relatively high column density for a low extinction (Object 10, $A_V = 5.75$, $N(\text{CO}) = 1.6 \times 10^{17}$ molecules cm⁻²), which may suggest that, with sufficient sensitivity, ices can be detected at lower A_V values than previously reported in the literature.

Figure 9b shows the column densities of CO₂ and CO plotted against the column density of H₂O. Overall, the data calculated in this study agree well with literature values; the relationships between H₂O, CO₂ and CO in molecular clouds and around YSOs are well established and it is important that new data continue to reinforce previous results. As expected, there is no clear relation between the H₂O and CO column densities, as the freeze-out and formation mechanisms of each species differ vastly. However, a linear correlation between the H₂O and CO₂ column densities is evident, indicating a potential link in the formation chemistry of these two species. It is possible that they both share a common chemical starting point; one route to H₂O formation involves H + OH (e.g. Cuppen & Herbst 2007), one route to CO₂ formation involves CO + OH (Oba et al. 2010; Ioppolo et al. 2011; Noble et al. 2011; Zins et al. 2011) and could account for the CO₂ ice observed in quiescent regions (Nummelin et al. 2001; Pontoppidan 2006). Recent experimental results show that the relative rates of these two reactions, if occurring concurrently, and if they were the only reactions producing H₂O and CO₂, would generate around 20 times more H₂O than CO₂, assuming that all the reagents were equally available (Noble et al. 2011). Obviously, these conditions may not be satisfied even in a quiescent line of sight. Figure 9b shows that the H₂O:CO₂ ratio is approximately 10:1, suggesting that other mechanisms must produce the remainder of the observed CO₂. Unlike the subset of background stars and low luminosity YSOs surveyed here, column density values for low and high mass YSOs tend to be much higher (e.g. Gibb et al. 2004; Pontoppidan et al. 2008); corroborating evidence that UV processing or longer timescales promote CO₂ formation via more complex CO₂ formation mechanisms.

Figure 10 is a ternary plot showing the relative column densities of all three species on a single plot. It includes fewer data points than Figure 9, simply because far fewer studies have been able to ascertain the abundances of all three species towards individual lines of sight. This figure clearly illustrates the range of background star data and column densities which were probed by this survey.

Looking more closely at the three major ice species, more can be learnt about their interlinking chemistries by considering the individual components of each. During this process, it is important to consider all available literature data in order to ascertain general correlations, rather than potentially drawing conclusions based on survey-specific trends. We first consider the relationship between H₂O column density and the column densities of pure CO (CO_{mc}) and CO in a H₂O-rich ice environment (CO_{rc}) in Figure 11.

It is postulated from laboratory experiments that these two CO ice environments promote very different ice chemistries: in the pure CO ice the reactions are dom-

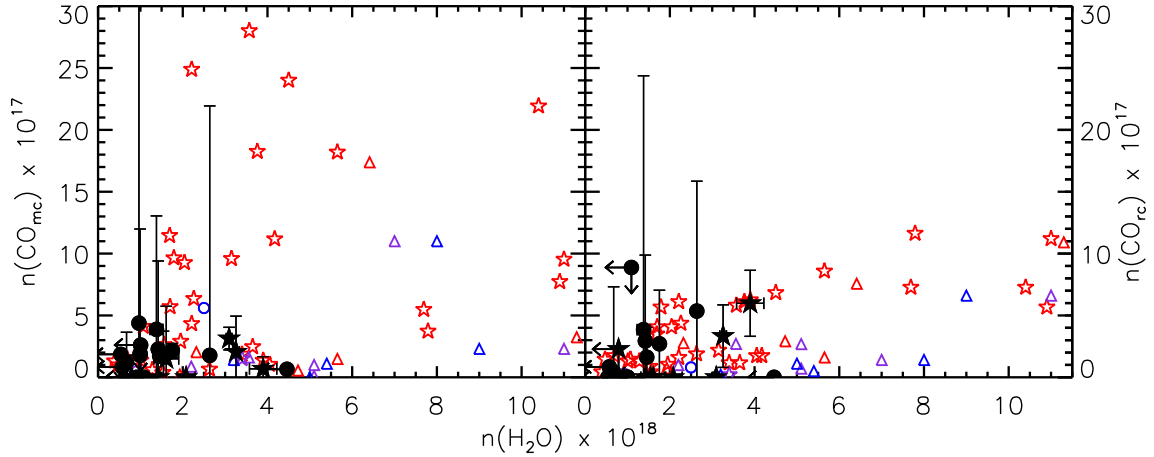


FIG. 11.— Correlation plots of CO components with H₂O. (Gerakines et al. 1999; Gibb et al. 2004; Pontoppidan et al. 2008).

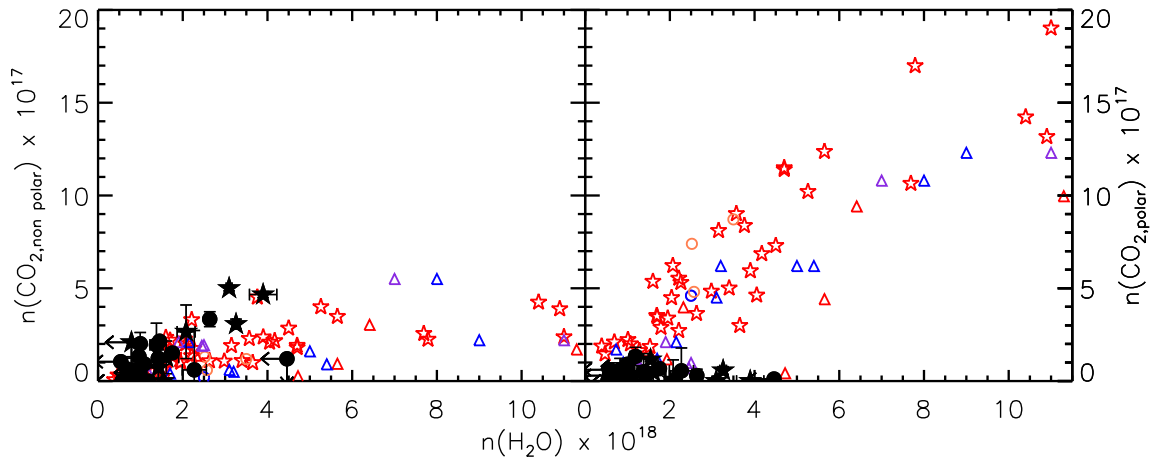


FIG. 12.— Correlation plots of CO₂ components with H₂O (Gerakines et al. 1999; Gibb et al. 2004; Pontoppidan et al. 2008; Whittet et al. 2009).

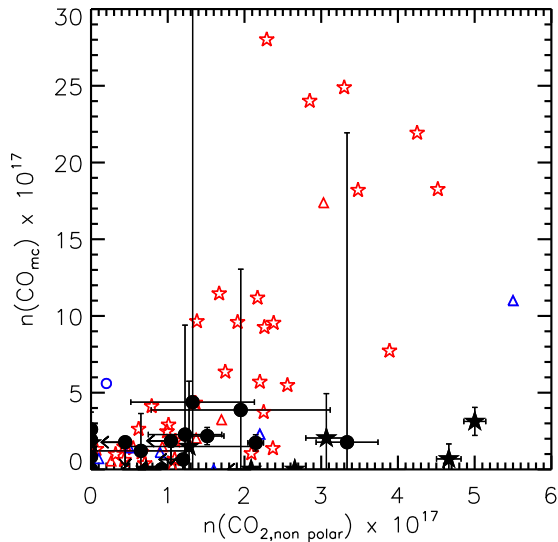


FIG. 13.— Correlation plot of CO_{mc} column density plotted against CO₂ in a CO-rich ice environment (Gerakines et al. 1999; Gibb et al. 2004; Pontoppidan et al. 2008).

inated by successive H atom, O atom and radical additions to the CO molecule to form CO₂, HCOOH, H₂CO and CH₃OH (e.g. Watanabe et al. 2004; Fuchs et al.

2009); in the water-rich CO ice, photon- and electron-induced chemical processes become more important, firstly because the CO molecule is trapped, leading to a CO chemistry at temperatures above its desorption energy, and secondly because (unlike the CO molecule) H₂O can be photodissociated, allowing reaction with CO to form CO₂, HCOOH, H₂CO and CH₃OH as well as many more complex molecules (e.g. Gerakines et al. 1996; Jamieson et al. 2006). It is only through observational evidence that we can start to discriminate between these processes and refine gas-grain astrochemical models.

It is clear from analysis of Figure 11 that there is no correlation of H₂O with pure CO, which condenses out of the gas phase as a layer on top of the H₂O. However, for the H₂O-rich phase of the CO, as expected, N(CO_{rc}) increases with N(H₂O). Collings et al. (2003a) offer evidence for the porosity of H₂O in the ISM, as their experiments suggest that the population of CO in a H₂O-rich environment develops upon heating of a layered system. A higher column density of H₂O ice suggests a larger number of pores for the CO to migrate into with time or temperature to produce a mixed phase (Pontoppidan et al. 2003a). As Figure 11 shows, towards YSOs there is generally a higher column density of CO in a H₂O-rich environment. The ice has been present in

these regions for longer, so it is therefore more likely that the CO has had the time (or the temperature change) necessary to migrate into a mixed H₂O layer. Otherwise, background stars would be expected to probe lines of sight with equally high column densities of CO_{rc}. It is important to note that CO_{rc} is a derived feature, as it can not be measured in isolation in the laboratory.

Figure 12 illustrates the relationship between the H₂O column density and that of the two components of CO₂ – CO₂ in a CO-rich ice (CO_{2,non polar}) and CO₂ in a H₂O-rich ice (CO_{2,polar}). When the component column densities from the broader literature, primarily from low and intermediate mass objects, are included in the plot (open symbols), two different correlation gradients are clearly evident, which both scale directly with ice abundance (albeit at different rates) suggesting that the dominant formation mechanisms for CO₂ in water-rich and water-poor environments are independent of one another. Whittet et al. (2009) generated similar gradient profiles by comparing the total elemental O atom distribution, derived by summing the CO, CO₂, and H₂O ice column densities, in the H₂O-rich (*polar*) and CO-rich (*apolar*) ice phases on extincted lines of sight towards a sample of around ten bright background stars and YSOs. They show that the elemental O is uniformly distributed between the water-rich and water-poor ice components, and is well correlated with the dust density, suggesting that the final fraction of O atoms accumulating in interstellar ices is a constant reservoir from cloud to cloud, but that the absolute source to source O atom distribution between the three major ice molecules – CO, H₂O, and CO₂ – can vary significantly. They attribute most of this variance to the CO₂ population in the water-rich ice component, suggesting that the CO₂ ice column densities are invariant with the efficiency of surface chemical pathways, instead reflecting variations in gas phase chemistry (related to CO gas densities) or photodesorption of the CO ice.

Our data do not entirely corroborate this conclusion. The component column densities of CO₂ in a CO-rich ice (CO_{2,non polar}), derived from our two-component fitting, match very well with previously reported values (as is the case for the CO ice components in Figure 11), providing reassurance in our analysis methods, despite the fitting limitations imposed by the AKARI resolution discussed in § 5.3. It is therefore interesting to note that we have sampled a very specific population of CO₂ in a H₂O-rich ice (CO_{2,polar}), which clearly occupy the lower left-hand region of Figure 12, commensurate with a handful of previous data points. It seems therefore that the formation of CO₂ in H₂O-rich ices is actually bimodal. The most likely scenario is that CO₂ ices first form via atom and radical surface reactions of CO in competition with H₂O formation, producing a limited concentration of CO₂ in a H₂O-rich ice (CO_{2,polar}). Later, a combination of CO freeze-out and CO migration to the water-rich ice layer, followed by energetic processing of the ices, leads to a second phase of CO₂ formation, which then dominates the CO₂ in a H₂O-rich ice (CO_{2,polar}) column density. This is entirely in agreement with the “early” and “late” formation mechanism model proposed by Öberg et al. (2011), and implies that the CO₂:H₂O ratio will vary significantly from source to source (as

indicated by Whittet et al. (2009)), but that this ratio will initially be dependent on competing surface reaction rates between CO, H, and OH to form CO₂ and H₂O, then subsequently on the degree to which ice mantles are thermally or energetically processed, rather than the prevailing gas phase conditions. Poteet et al. (2013) have very recently illustrated that crystalline CO₂-rich ice layers can dominate grain mantles under the unusual circumstances where significant thermal processing occurs in the vicinity of a protostar (in this case HOPS-68). On the one hand, therefore, Figure 12 corroborates the Whittet et al. (2009) hypothesis: the component of CO₂ ice in the H₂O-rich layer dominates the correlations between the major interstellar ice components. However, whilst our overall CO₂ column densities match well with existing literature values, the fraction of CO₂ ice we observe in water-rich environments is relatively small.

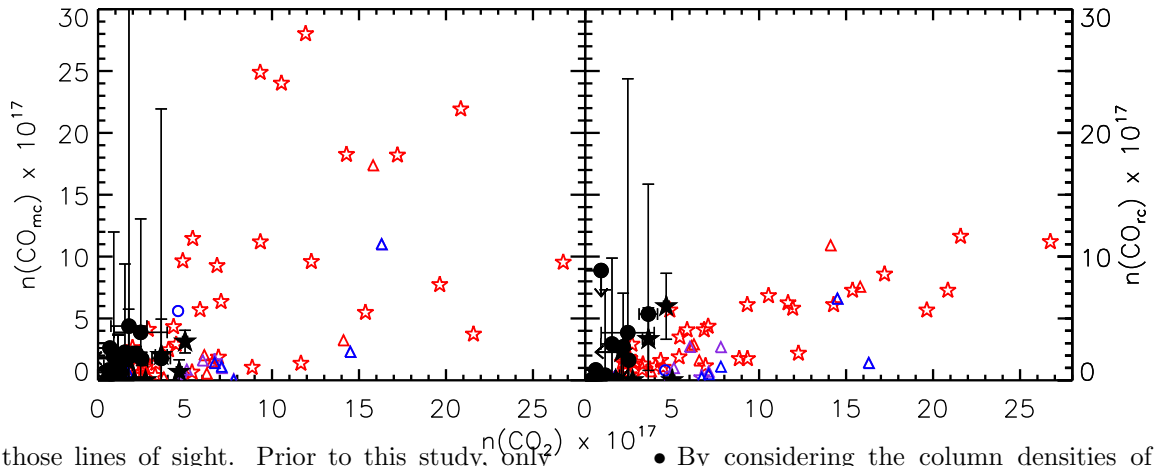
Previous studies have illustrated that there is not a direct link between CO freeze-out and all CO₂ formation, as there is no overall correlation in the abundances of total CO and total CO₂ (e.g. Gerakines et al. 1999). In Figure 13, the plot of the pure component of CO against the CO-rich component of CO₂ shows no correlation, suggesting that the formation route to CO₂ formed in the CO layer is not a simple one, and probably not driven only by CO reacting with O, H, or OH from the gas phase; a similar conclusion was reached from our analysis of Figure 9b. It is likely that the relative CO and CO₂ populations in the CO-rich ice environments are additionally regulated by competing photo-desorption processes (e.g. Öberg et al. 2007, 2009; Fayolle et al. 2011).

Figure 14 shows plots of the column density of the water-rich CO₂ component versus the column density of the CO components CO_{mc} and CO_{rc}. It is very clear from these plots that there is a strong link between the column densities of CO₂ and CO in a H₂O-rich environment (CO_{rc}). Thus, some CO₂ must form from CO in a H₂O environment. Mirroring the relationship established between H₂O and CO₂ in a H₂O-rich environment (Figure 12), background stars probing quiescent lines of sight have the lowest column densities of CO in a H₂O-rich environment, while in the more evolved YSOs, there is a higher column density, suggesting that CO₂ forms from CO which has migrated into the H₂O upon formation of a star in the core. This is key evidence supporting the conclusions of the ice mapping in Pontoppidan (2006).

These data illustrate the links between all of the components present in the CO and CO₂ absorption features, and the sequence of CO₂ formation in molecular clouds and star-forming cores. The proposed sequence is outlined here: initially, CO₂ forms concurrently with H₂O, producing an abundance of CO₂ in H₂O. Upon critical freeze-out of CO, further CO₂ is formed by reactions of CO with O, H, and OH, producing a CO₂ component in a CO-rich ice. With time and, potentially, processing, some CO migrates into the H₂O ice, where it can react to form large column densities of CO₂ in a H₂O-rich ice, likely by an energetic route enhanced by UV radiation from a newly formed YSO.

7. CONCLUSIONS

In this paper, the 2.5 – 5 μ m spectra of 22 background stars and eight YSOs have been analysed to determine the column densities of key solid phase molecular species



towards those lines of sight. Prior to this study, only one complete spectrum of a background star had been obtained in this wavelength region, a region containing absorption bands for the three most abundant molecules present in interstellar ice. Thus, the addition of 22 spectra towards background stars to the literature provides valuable data to the community, which could help to benchmark the initial conditions in star-forming regions before the onset of star formation.

The analysis of this large sample of data by a rigorous fitting approach reinforces the argument that the methods employed here are possible for large datasets (as previously shown by e.g. Pontoppidan et al. 2003a, 2008; Boogert et al. 2008; Öberg et al. 2011). It is not necessary to employ a “mix and match” approach using multiple laboratory spectra in order to define the ice characteristics of a wide range of objects.

In summary, the key findings of this survey are:

- The sensitivity of AKARI enabled us to probe lines of sight towards objects with fluxes < 5 mJy, allowing observation of spectra in a previously inaccessible parameter space.
- CO₂ and H₂O were found to be ubiquitous where ice was observed, at column densities commensurate with previously reported literature values.
- From the profile of the H₂O ice band, the extended red wing seems to be an evolutionary indicator of both dust properties and the extent to which the ice mantle covers the grain.
- New observations of the CO₂ stretching absorption band profiles, and ice column densities for lines of sight towards 21 background stars, have been obtained.
- CO ice absorption features were extracted from the spectra of 23 of the 30 lines of sight probed. In at least two objects – Objects 4 and 20 – the CO ice absorption band profile is fully described by a single pure CO component only.
- On 15 lines of sight towards background stars, the column densities of all three species H₂O, CO₂, and CO were extracted.

- By considering the column densities of CO and CO₂ in different ice components, it is possible to postulate a CO₂ formation scenario involving two or three distinct stages. The proposed timeline is: early formation concurrent with H₂O; late formation by energetic routes when CO has frozen out and migrated into an H₂O environment; and the formation of CO₂ in the CO layer at an uncertain time, and by uncertain mechanisms.

As our knowledge of interstellar solid state ices increases, many common factors are continuing to emerge in our understanding of their formation and evolution. By surveying ices features in the spectra of faint YSOs and background sources, we have sampled a further region of parameter space in which ices can be detected. Clearly, even where correlations are evident between one ice species and another, the range of molecular column densities remains vast. The local environment must, therefore, have a significant effect on ice column density, composition and growth. Even the individual components of a species potentially vary across a cloud. In order to use solid phase molecular species as probes of ice and gas chemistry, it will be necessary to map their distributions on a 2D spatial scale, as well as making many more observations of both solid phase species and gas phase molecules.

The authors are very grateful to Y. Ohyama for fruitful discussions, and thank M. Tamura, M. Ueno, R. Kandori, and A. Kawamura for their help with the initial target selection of the ISICE programme. J.A.N. is a Royal Commission for the Exhibition of 1851 Research Fellow, and acknowledges the financial support of the University of Strathclyde, the Scottish Universities Physics Alliance, and the Japan Society for the Promotion of Science. The research leading to these results has received funding from the European Community’s Seventh Framework Programme FP7/2007-2013 under grant agreement No. 238258 (LASSIE). H.J.F. and J.A.N. are grateful to EU funded COST Action CM0805 “The Chemical Cosmos: Understanding Chemistry in Astronomical Environments” for a funding contribution towards the final production of this work.

Facilities: AKARI.

REFERENCES

- Alexander, R. D., Casali, M. M., André, P., Persi, P., & Eiroa, C. 2003, *A&A*, 401, 613
- ASTRO-F User Support Team 2005, *ASTRO-F Observer's Manual*. Version 3.0, Sagami-hara, Japan, <http://www.ir.isas.jaxa.jp/ASTRO-F/Observation/ObsMan/afobsman100.pdf>
- Bergin, E. A., Melnick, G. J., Gerakines, P. A., Neufeld, D. A., & Whittet, D. C. B. 2005, *ApJ*, 627, L33
- Bohren, C. F., Huffman D. R., 1983, *Absorption and Scattering of Light by Small Particles*. John Wiley & Sons, New York, Ch. 5
- Boogert, A. C. A., & Ehrenfreund, P. 2004, *Astrophysics of Dust*, 309, 547
- Boogert, A. C. A., Ehrenfreund, P., Gerakines, P. A., et al. 2000, *A&A*, 353, 349
- Boogert, A. C. A., Huard, T. L., Cook, A. M., et al. 2011, *ApJ*, 729, 92
- Boogert, A. C. A., Pontoppidan, K. M., Knez, C., et al. 2008, *ApJ*, 678, 985
- Bottinelli, S., Boogert, A. C. A., Bouwman, J., et al. 2010, *ApJ*, 718, 1100
- Brooke, T. Y., Sellgren, K., & Geballe, T. R. 1999, *ApJ*, 517, 883
- Burgdorf, M., Cruikshank, D. P., Dalle Ore, C. M., et al. 2010, *ApJ*, 718, L53
- Chapman, N. L., & Mundy, L. G. 2009, *ApJ*, 699, 1866
- Chiar, J. E., Adamson, A. J., Kerr, T. H., & Whittet, D. C. B. 1994, *ApJ*, 426, 240
- Chiar, J. E., Adamson, A. J., Kerr, T. H., & Whittet, D. C. B. 1995, *ApJ*, 455, 234
- Chiar, J. E., Pendleton, Y. J., Allamandola, L. J., et al. 2011, *ApJ*, 731, 9
- Cohen, M., Walker, R. G., Carter, B., et al. 1999, *AJ*, 117, 1864
- Collings, M. P., Dever, J. W., Fraser, H. J., McCoustra, M. R. S., & Williams, D. A. 2003a, *ApJ*, 583, 1058
- Collings, M. P., Dever, J. W., Fraser, H. J., & McCoustra, M. R. S. 2003b, *Ap&SS*, 285, 633
- Cottin, H., Moore, M. H., & Bénilan, Y. 2003, *ApJ*, 590, 874
- Cuppen, H. M., & Herbst, E. 2007, *ApJ*, 668, 294
- Cuppen, H. M., Pentead, E. M., Isokoski, K., van der Marel, N., & Linnartz, H. 2011, *MNRAS*, 417, 2809
- Dartois, E., d'Hendecourt, L., Thi, W., Pontoppidan, K. M., & van Dishoeck, E. F. 2002, *A&A*, 394, 1057
- Dartois, E., Thi, W.-F., Geballe, T. R., et al. 2003, *A&A*, 399, 1009
- de Graauw, T., Whittet, D. C. B., Gerakines, P. A., et al. 1996, *A&A*, 315, L345
- Dulieu, F., Amiaud, L., Congiu, E., et al. 2010, *A&A*, 512, A30
- Ehrenfreund, P., Boogert, A. C. A., Gerakines, P. A., et al. 1996, *A&A*, 315, L341
- Ehrenfreund, P., Boogert, A. C. A., Gerakines, P. A., et al. 1997, *A&A*, 328, 649
- Eiroa, C., & Hodapp, K.-W. 1989, *A&A*, 210, 345
- Evans, N. J., II, Allen, L. E.; Blake, G. A., et al. 2003, *PASP*, 115, 965
- Fayolle, E. C., Öberg, K. I., Cuppen, H. M., Visser, R., & Linnartz, H., 2011, *A&A*, 529, A74
- Fraser, H. J., & van Dishoeck, E. F. 2004, *Advances in Space Research*, 33, 14
- Fraser, H. J., Bisschop, S. E., Pontoppidan, K. M., Tielens, A. G. G. M., & van Dishoeck, E. F. 2005, *MNRAS*, 356, 1283
- Fuchs, G. W., Cuppen, H. M., Ioppolo, S., et al. 2009, *A&A*, 505, 629
- Gerakines, P. A., Schutte, W. A., & Ehrenfreund, P. 1996, *A&A*, 312, 289
- Gerakines, P. A., Schutte, W. A., Greenberg, J. M., & van Dishoeck, E. F. 1995, *A&A*, 296, 810
- Gerakines, P. A., Whittet, D. C. B., Ehrenfreund, P., et al. 1999, *ApJ*, 522, 357
- Gibb, E. L., Whittet, D. C. B., Boogert, A. C. A. & Tielens, A. G. G. M. 2004, *ApJS*, 151, 35
- Goumans, T. P. M., Uppal, M. A., & Brown, W. A. 2008, *MNRAS*, 384, 1158
- Guertler, J., Henning, T., Koempe, C., et al. 1996, *A&A*, 315, L189
- Hagen, W., Allamandola, L. J., & Greenberg, J. M. 1980, *A&A*, 86, L3
- Hauschildt, P. H., Allard, F., & Baron, E. 1999, *ApJ*, 512, 377
- Honda, M., Inoue, A. K., Fukagawa, M., et al. 2009, *ApJ*, 690, L110
- Ioppolo, S., Cuppen, H. M., Romanzin, C., van Dishoeck, E. F., & Linnartz, H. 2008, *ApJ*, 686, 1474
- Ioppolo, S., van Boheemen, Y., Cuppen, H. M., van Dishoeck, E. F., & Linnartz, H. 2011, *MNRAS*, 413, 2281
- Itoh, Y., Tamura, M., & Gatley, I. 1996, *ApJ*, 465, L129
- Jamieson, C. S., Mebel, A. M., & Kaiser, R. I. 2006, *ApJS*, 163, 184
- Jones, A. P. 2012, *A&A*, 540, A1
- Kandori, R., Dobashi, K., Uehara, H., Sato, F., & Yanagisawa, K. 2003, *AJ*, 126, 1888
- Knez, C., Boogert, A. C. A., Pontoppidan, K. M., et al. 2005, *ApJ*, 635, L145
- Landsman, W. B. 1993, *Astronomical Data Analysis Software and Systems II*, 52, 246
- Leger, A., Klein, J., de Cheveigne, S., et al. 1979, *A&A*, 79, 256
- Malfait, K., Waelkens, C., Waters, L. B. F. M., et al. 1998, *A&A*, 332, L25
- Markwardt, C. B. 2009, *Astronomical Society of the Pacific Conference Series*, 411, 251
- Mennella, V., Palumbo, M. E., & Baratta, G. A. 2004, *ApJ*, 615, 1073
- Miyauchi, N., Hidaka, H., Chigai, T., et al. 2008, *Chemical Physics Letters*, 456, 27
- Murakawa, K., Tamura, M., & Nagata, T. 2000, *ApJS*, 128, 603
- Noble, J. A. 2011, Ph.D. Thesis, University of Strathclyde
- Noble, J. A., Dulieu, F., Congiu, E., & Fraser, H. J. 2011, *ApJ*, 735, 121
- Nummelin, A., Whittet, D. C. B., Gibb, E. L., Gerakines, P. A., & Chiar, J. E. 2001, *ApJ*, 558, 185
- Oba, Y., Watanabe, N., Kouchi, A., Hama, T., & Pirronello, V. 2010, *ApJ*, 712, L174
- Öberg, K. I., Boogert, A. C. A., Pontoppidan, K. M., et al. 2008, *ApJ*, 678, 1032
- Öberg, K. I., Boogert, A. C. A., Pontoppidan, K. M., et al. 2011, *ApJ*, 740, 109
- Öberg, K. I., Fuchs, G. W., Awad, Z., et al. 2007, *ApJ*, 662, L23
- Öberg, K. I., van Dishoeck, E. F., & Linnartz, H., 2009, *A&A*, 496, 281
- Ohyama, Y., Onaka, T., Matsuhara, H., et al. 2007, *PASJ*, 59, 411
- Oliveira, J. M., van Loon, J. Th., Sloan, G. C., et al. 2011, *MNRAS*, 411, L36
- Onaka, T., Matsuhara, H., Wada, T., et al. 2007, *PASJ*, 59, 401
- Onaka, T., Sakon, I., Ohsawa, R., et al. 2011, *EAS Publications Series*, 46, 55
- Palumbo, M. E., Baratta, G. A., Brucato, J. R., et al. 1998, *A&A*, 334, 247
- Pontoppidan, K. M. 2006, *A&A*, 453, L47
- Pontoppidan, K. M., Boogert, A. C. A., Fraser, H. J., et al. 2008, *ApJ*, 678, 1005
- Pontoppidan, K. M., Fraser, H. J., Dartois, E., et al. 2003a, *A&A*, 408, 981
- Pontoppidan, K. M., Dartois, E., van Dishoeck, E. F., Thi, W.-F., & d'Hendecourt, L. 2003b, *A&A*, 404, L17
- Pontoppidan, K. M., van Dishoeck, E. F., & Dartois, E. 2004, *A&A*, 426, 925
- Poteet, C. A., Pontoppidan, K. M., Megeath, S. T., et al. 2013, *ApJ*, 766, 117
- Román-Zúñiga, C. G., Lada, C. J., Muench, A., & Alves, J. F. 2007, *ApJ*, 664, 357
- Sakon, I., Onaka, T., Ootsubo, T., Matsuhara, H. & Noble, J. A. 2012, *Proc. SPIE*, 8442, 844244-1-9
- Sandford, S. A., Bernstein, M. P., Allamandola, L. J., Goorvitch, D., & Teixeira, T. C. V. S. 2001, *ApJ*, 548, 836
- Shenoy, S. S., Whittet, D. C. B., Ives, J. A., & Watson, D. M. 2008, *ApJS*, 176, 457
- Shimonishi, T., Onaka, T., Kato, D., et al. 2008, *ApJ*, 686, L99
- Shimonishi, T., Onaka, T., Kato, D., et al. 2010, *A&A*, 514, A12
- Shuping, R. Y., Snow, T. P., Chiar, J. E., & Kerr, T. 2000, *ApJ*, 529, 932
- Smith, R. G., Sellgren, K., & Tokunaga, A. T. 1989, *ApJ*, 344, 413
- Smith, R. G., Sellgren, K., & Brooke, T. Y. 1993, *MNRAS*, 263, 749
- Sorahana, S., & Yamamura, I. 2012, *ApJ*, 760, 151

- Tanaka, M., Sato, S., Nagata, T., & Yamamoto, T. 1990, *ApJ*, 352, 724
- Thi, W.-F., van Dishoeck, E. F., Dartois, E., et al. 2006, *A&A*, 449, 251
- Tielens, A. G. G. M., & Hagen, W. 1982, *A&A*, 114, 245
- Tielens, A. G. G. M., Tokunaga, A. T., Geballe, T. R., & Baas, F. 1991, *ApJ*, 381, 181
- van Broekhuizen, F. A., Groot, I. M. N., Fraser, H. J., van Dishoeck, E. F., & Schlemmer, S. 2006, *A&A*, 451, 723
- van Broekhuizen, F. A., Keane, J. V., & Schutte, W. A. 2004, *A&A*, 415, 425
- van Broekhuizen, F. A., Pontoppidan, K. M., Fraser, H. J., & van Dishoeck, E. F. 2005, *A&A*, 441, 249
- van Dishoeck, E. F., Helmich, F. P., de Graauw, T., et al. 1996, *A&A*, 315, L349
- van Kempen, T. A., van Dishoeck, E. F., Güsten, R., et al. 2009, *A&A*, 501, 633
- Watanabe, N., Nagaoka, A., Shiraki, T., & Kouchi, A. 2004, *ApJ*, 616, 638
- Weingartner, J. C., & Draine, B. T. 2001, *ApJ*, 548, 296
- Whittet, D. C. B., Adamson, A. J., Duley, W. W., Geballe, T. R., & McFadzean, A. D. 1989, *MNRAS*, 241, 707
- Whittet, D. C. B., Bode, M. F., Baines, D. W. T., Longmore, A. J., & Evans, A. 1983, *Nature*, 303, 218
- Whittet, D. C. B., Bode, M. F., Longmore, A. J., et al. 1988, *MNRAS*, 233, 321
- Whittet, D. C. B., Cook, A. M., Chiar, J. E., et al. 2009, *ApJ*, 695, 94
- Whittet, D. C. B., & Duley, W. W. 1991, *A&A Rev.*, 2, 167
- Whittet, D. C. B., Gerakines, P. A., Tielens, A. G. G. M., et al. 1998, *ApJ*, 498, L159
- Whittet, D. C. B., McFadzean, A. D., & Longmore, A. J. 1985, *MNRAS*, 216, 45P
- Whittet, D. C. B., Pendleton, Y. J., Gibb, E. L., et al. 2001, *ApJ*, 550, 793
- Whittet, D. C. B., Shenoy, S. S., Bergin, E. A., et al. 2007, *ApJ*, 655, 332
- Yamagishi, M., Kaneda, H., Ishihara, D., et al. 2011, *ApJ*, 731, L20
- Zasowski, G., Kemper, F., Watson, D. M., et al. 2009, *ApJ*, 694, 459
- Zins, E.-L., Joshi, P. R., & Krim, L. 2011, *ApJ*, 738, 175